UNDERGRADUATE RESEARCH PROGRAM

2018

UCLA Samueli
School of Engineering

DEAN'S MESSAGE

The Undergraduate Research Program's (URP) mission is to provide participants with research experience in a wide range of engineering fields. Undergraduate students participate in research with UCLA Samueli School of Engineering faculty and research teams to gain real-world lab experience. As part of this program, URP students:

- Meet and network with peers who have similar goals and interests
- Learn to communicate research outcomes by participating in weekly Journal Club meetings
- Create a professional scientific poster of their research
- Write and publish a research abstract
- Present a detailed Summary of Project
- Become more competitive when applying to engineering graduate schools

This year, 23 Samueli undergraduate students were selected to join the first-ever URP cohort. I would like to congratulate this inaugural URP class on completion of their amazing research projects. Creating new knowledge is a very important, and very difficult, task. These high-performing students have done an outstanding job balancing their normal academic course load with the rigorous demands of research. They should be very proud of the abstracts and posters they have published today. I encourage you to meet the students, ask questions about their projects, and learn about the amazing new knowledge that is being created here at the UCLA Samueli School of Engineering.

Sincerely,

Jayathi Murthy
Ronald and Valerie Sugar Dean

Daniel Chien

Bioengineering

Senior

LAB NAME

The Ozcan Research Group

FACULTY ADVISOR

Aydogan Ozcan

DAILY LAB SUPERVISOR

Mustafa Daloğlu

DEPARTMENT

Electrical Engineering

3D Sperm Tail Tracking and Holographic Reconstruction

Recently, researchers have utilized a lensfree on-chip imaging technique to track 3D human sperm trajectories. This technique relies on acquiring holographic lensfree shadows of sperms at two different wavelengths that originate from two partially-coherent sources placed at 45 degrees with respect to one another. Due to being able to observe the 3D sperm trajectories, researchers could also collect different types of data for various parameters of 3D swimming patterns such as curvilinear velocity (VCL), straight-line velocity (VSL), amplitude of lateral head displacement (ALH), beat-cross frequency (BCF), and linearity. We have been using this technique to image bovine sperm trajectories specifically to investigate whether there is a difference between X karyotype and Y karyotype sperm. We conducted multiple experiments over the summer to capture many sperm trajectories. Our studies thus decided to focus on 3D morphological differences of X and Y sperm.

High-throughput 3D Tracking of Sperm Cells

Francis Lin, Bryan Chong, Daniel Chien, Mustafa Ugur Daloglu, Muhammed Veli and Aydogan Ozcan

Departments of Bioengineering, and Electrical Engineering, University of California, Los Angeles, CA 90095 USA

org.ee.ucla.edu innovate.ee.ucla.edu ozcan@ucla.edu

Introduction

The 3D trajectories and swimming patterns of microswimmers reveal the underlying physical and chemical principles that govern their movement, and sheds light on the evolution of the organisms. However, dynamic tracking of microswimmers over a large volume is a challenging task because conventional lens-based optical microscopes have limited imaging volumes. Human sperms, for example, are 3 to 4 micrometers in head size and move at speeds of 20 to 100 micrometers/s, making it impractical to perform 3D tracking using a lens-based microscope which has a typical field-of-view (FOV) diameter of 0.4 mm and focal depth of several micrometers; the specimen can quickly move away from the microscope's focal plane or observation area.

We report a lensfree on-chip holographic imaging platform that is especially suitable for wide field 3D tracking because it provides an unparalleled wide FOV with sub-micron localization accuracy. Using dual angle illuminations, our platform tracks individual 3D trajectories of over 1000 sperms at sub-micron accuracy within a large sample volume (~9 mL) at a frame rate of >140 frames per second. It provides two important features that are lacking in the current study of microswimmers: (1) sub-micron accurate 3D trajectories over a long period; (2) statistics of a large number of trajectories. To extend our capabilities in tracking high velocity microswimmers, such as bovine sperm, the frame readout speed was increased to 300 frame per second, maintaining details of the trajectory that would have been lost due to undersampling otherwise. These results are of great interest for biophysics: a large amount of data with high accuracy enables us to discover rare events such as helical trajectories of sperms and obtain their statistical characteristics.

Methods

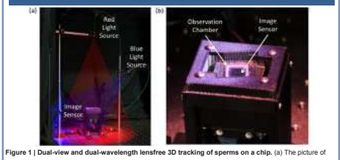

Figure 1 | Dual-view and dual-wavelength lensfree 3D tracking of sperms on a chip. (a) The picture of the imaging system. Two partially-coherent light sources (LED-coupled multimode fibers, core size: 400 mm) illuminate the observation chamber from two different angles with two different wavelengths (vertical one: 625 nm; oblique one at 45u: 470 nm; bandwidth .20 nm). A CMOS image sensor records the dual-view lensfree holograms that encode the position information of each sperm. (b) The close-up image of an observation chamber that is placed on the top of the CMOS image sensor.

Methods (Cont'd)

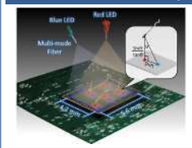

Figure 2 | The schematic diagram of the imaging system. The 3D location of each sperm is determined by the centroids of its head images reconstructed in the vertical (red) and oblique (blue) channels.

Results

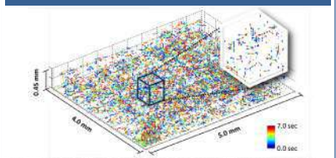

Figure 3 | Reconstructed 3D spatio-temporal trajectories of sperms. 998 horse sperms were tracked inside a volume of 9.0 mL at a frame rate of 143 FPS. The time position of each track point is encoded by its color.

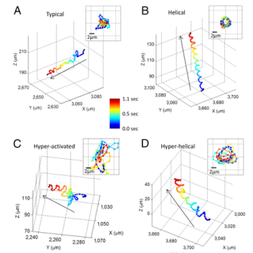

Figure 4 | Four major categories of human sperm swimming patterns. (A) The typical pattern. (B) The helical pattern. (C) The hyperactivated pattern. (D) The hyperhelical pattern. The helices shown in (B) and (D) are both right-handed.

Results (Cont'd)

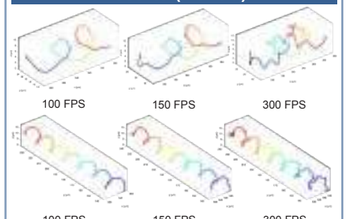

Figure 5 | Frame rate comparison in 3D bovine sperm trajectories. A high frame rate, ~300 FPS, is required to capture 3D bovine sperm trajectories without loss of detail due to undersampling. This effect is demonstrated by numerically reducing the sampling rate of bovine sperm trajectories captured at the full frame rate of 300 FPS by a factor of 2 and 3 resulting in an effective sampling rate of 150 FPS and 100 FPS respectively. The gradual loss of detail in the trajectories is visible with the decreasing sampling rate.

References

1. T-W. Su, L. Xue and A. Ozcan, "High-throughput lensfree 3D tracking of human sperms reveals rare statistics of helical trajectories," Proceedings of the National Academy of Sciences (PNAS) (2012)
2. T-W. Su, I. Choi, J. Feng, K. Huang, E. McLeod, and A. Ozcan, "Sperm Trajectories Form Chiral Ribbons," Scientific Reports (Nature Publishing Group) (2013)
3. T-W. Su, I. Choi, J. Feng, K. Huang, W. Luo, A. Ozcan, "High-throughput on-chip analysis of 3D swimming patterns of animal sperms using holographic lensfree imaging," SPIE Photonics West, 2015

Acknowledgements

We thank the Howard Hughes Undergraduate Research Program for their funding and support . The authors acknowledge the support of the Presidential Early Career Award for Scientists and Engineers (PECASE), Army Research Office (ARO) Life Sciences Division (W911NF-13-1-0419 and W911NF-13-1-0197), ARO Young Investigator Award, National Science Foundation (NSF) CAREER Award, NSF CBET Division Biophotonics Program, NSF Emerging Frontiers in Research and Innovation (EFRI) Award, NSF EAGER Award, Office of Naval Research (ONR), the Howard Hughes Medical Institute (HHMI), and the DoE grant DE-SC0010064.

Ashley Clemens

Biochemistry

Junior

LAB NAME

The Ozcan Research Group

FACULTY ADVISOR

Aydogan Ozcan

DAILY LAB SUPERVISOR

Zach Ballard

DEPARTMENT

Electrical Engineering

Plasmonic Sensors for Detecting Lactoferrin on a Contact Lens

Localized resonance plasmonic sensing (LSPR) has been well-documented as a sensitive way to detect biomolecules, even down to the single molecule. LSPR sensors have also recently been demonstrated to be fabricated with low-cost and scalable fabrication techniques on flexible materials. In this work, we explore the use of LSPR sensors embedded in contact lenses for detecting the protein Lactoferrin in human tear fluid. By performing surface chemistry to immobilize Lactoferrin antibody on our LSRP sensors, we can then transfer the sensor to a contact lens where it specifically captures Lactoferrin in vivo, before the contact lens is removed and analyzed with a low-cost, field portable plasmonic sensor reader. Taken together with the low-cost reader, this wearable sensor can be used for point of care analysis for a previously inaccessible biofluid.

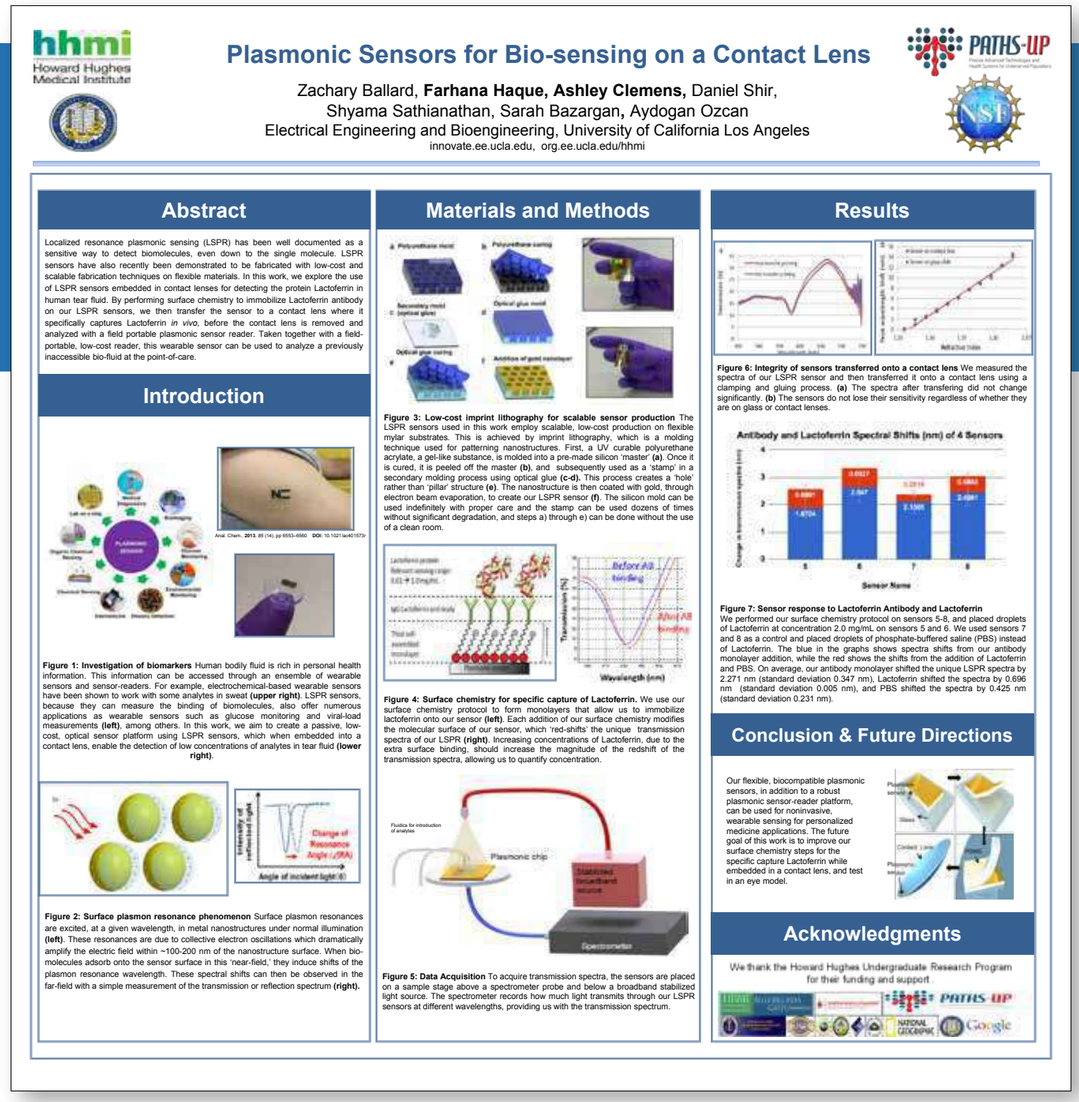

Plasmonic Sensors for Bio-sensing on a Contact Lens

Zachary Ballard, **Farhana Haque, Ashley Clemens,** Daniel Shir,
Shyama Sathianathan, Sarah Bazargan, Aydogan Ozcan
Electrical Engineering and Bioengineering, University of California Los Angeles
innovate.ee.ucla.edu, org.ee.ucla.edu/hhmi

Abstract

Localized resonance plasmonic sensing (LSPR) has been well documented as a sensitive way to detect biomolecules, even down to the single molecule. LSPR sensors have also recently been demonstrated to be fabricated with low-cost and scalable fabrication techniques on flexible materials. In this work, we explore the use of LSPR sensors embedded in contact lenses for detecting the protein Lactoferrin in human tear fluid. By performing surface chemistry to immobilize Lactoferrin antibody on our LSPR sensors, we then transfer the sensor to a contact lens where it specifically captures Lactoferrin *in vivo*, before the contact lens is removed and analyzed with a field portable plasmonic sensor reader. Taken together with a field-portable, low-cost reader, this wearable sensor can be used to analyze a previously inaccessible bio-fluid at the point-of-care.

Introduction

Anal. Chem., **2013**, 85 (14), pp 6553–6560 **DOI:** 10.1021/ac401573r

Figure 1: Investigation of biomarkers Human bodily fluid is rich in personal health information. This information can be accessed through an ensemble of wearable sensors and sensor-readers. For example, electrochemical-based wearable sensors have been shown to work with some analytes in sweat **(upper right)**. LSPR sensors, because they can measure the binding of biomolecules, also offer numerous applications as wearable sensors such as glucose monitoring and viral-load measurements **(left)**, among others. In this work, we aim to create a passive, low-cost, optical sensor platform using LSPR sensors, which when embedded into a contact lens, enable the detection of low concentrations of analytes in tear fluid **(lower right)**.

Figure 2: Surface plasmon resonance phenomenon Surface plasmon resonances are excited, at a given wavelength, in metal nanostructures under normal illumination **(left)**. These resonances are due to collective electron oscillations which dramatically amplify the electric field within ~100-200 nm of the nanostructure surface. When bio-molecules adsorb onto the sensor surface in this 'near-field,' they induce shifts of the plasmon resonance wavelength. These spectral shifts can then be observed in the far-field with a simple measurement of the transmission or reflection spectrum **(right)**.

Materials and Methods

Figure 3: Low-cost imprint lithography for scalable sensor production The LSPR sensors used in this work employ scalable, low-cost production on flexible mylar substrates. This is achieved by imprint lithography, which is a molding technique used for patterning nanostructures. First, a UV curable polyurethane acrylate, a gel-like substance, is molded into a pre-made silicon 'master' **(a)**. Once it is cured, it is peeled off the master **(b)**, and subsequently used as a 'stamp' in a secondary molding process using optical glue **(c-d)**. This process creates a 'hole' rather than 'pillar' structure **(e)**. The nanostructure is then coated with gold, through electron beam evaporation, to create our LSPR sensor **(f)**. The silicon mold can be used indefinitely with proper care and the stamp can be used dozens of times without significant degradation, and steps a) through e) can be done without the use of a clean room.

Figure 4: Surface chemistry for specific capture of Lactoferrin. We use our surface chemistry protocol to form monolayers that allow us to immobilize lactoferrin onto our sensor **(left)**. Each addition of our surface chemistry modifies the molecular surface of our sensor, which 'red-shifts' the unique transmission spectra of our LSPR **(right)**. Increasing concentrations of Lactoferrin, due to the extra surface binding, should increase the magnitude of the redshift of the transmission spectra, allowing us to quantify concentration.

Figure 5: Data Acquisition To acquire transmission spectra, the sensors are placed on a sample stage above a spectrometer probe and below a broadband stabilized light source. The spectrometer records how much light transmits through our LSPR sensors at different wavelengths, providing us with the transmission spectrum.

Results

Figure 6: Integrity of sensors transferred onto a contact lens We measured the spectra of our LSPR sensor and then transferred it onto a contact lens using a clamping and gluing process. **(a)** The spectra after transfering did not change significantly. **(b)** The sensors do not lose their sensitivity regardless of whether they are on glass or contact lenses.

Figure 7: Sensor response to Lactoferrin Antibody and Lactoferrin
We performed our surface chemistry protocol on sensors 5-8, and placed droplets of Lactoferrin at concentration 2.0 mg/mL on sensors 5 and 6. We used sensors 7 and 8 as a control and placed droplets of phosphate-buffered saline (PBS) instead of Lactoferrin. The blue in the graphs shows spectra shifts from our antibody monolayer addition, while the red shows the shifts from the addition of Lactoferrin and PBS. On average, our antibody monolayer shifted the unique LSPR spectra by 2.271 nm (standard deviation 0.347 nm), Lactoferrin shifted the spectra by 0.696 nm (standard deviation 0.005 nm), and PBS shifted the spectra by 0.425 nm (standard deviation 0.231 nm).

Conclusion & Future Directions

Our flexible, biocompatible plasmonic sensors, in addition to a robust plasmonic sensor-reader platform, can be used for noninvasive, wearable sensing for personalized medicine applications. The future goal of this work is to improve our surface chemistry steps for the specific capture Lactoferrin while embedded in a contact lens, and test in an eye model.

Acknowledgments

We thank the Howard Hughes Undergraduate Research Program for their funding and support.

Ali Farhat

Bioengineering

Junior

LAB NAME
Meyer Lab

FACULTY ADVISOR
Aaron Meyer

DAILY LAB SUPERVISOR
None

DEPARTMENT
Bioengineering

Mapping Common Gamma Chain Cytokine Receptor Input-Output Behavior with Tensor Factorization

Cytokines are cell signaling proteins responsible for communication within the immune system. The common gamma chain cytokine receptors, ligands of which include IL2, IL7, IL9, and IL15, are integral for modulating both innate and adaptive immune responses and have accrued broad interest for their potential as immune therapies. The complex binding activation mechanism of these receptors, wherein a single common receptor must complex with a series of private receptors, makes rationally engineering and manipulating the activity of these receptors challenging. Further, the effects of any intervention operate across multiple distinct cell populations with unique responses to these cytokines as a consequence of their receptor expression. For this project, we utilize computational modeling on both ligand-receptor interactions and endosomal receptor trafficking in order to study each ligand's effects on receptor activation. By fitting the model to experimental measurements, we computationally solve the input-output behavior of cytokine response. We finally visualize the effect cytokine stimulation has across individual immune cell populations using tensor factorization. This map of the signaling landscape for this receptor family will guide further immune therapy development.

Mapping Common Gamma Chain Cytokine Receptor Input-Output Behavior with Tensor Factorization

Ali Farhat, Adam Weiner, Aaron Meyer

Meyer Lab, Department of Bioengineering

UCLA

Introduction

Cytokines are cell signaling proteins responsible for communication within the immune system. The common gamma chain cytokine receptors, ligands of which include IL2, IL7, IL9, and IL15, are integral for modulating both innate and adaptive immune responses and have accrued broad interest for their potential as immune therapies. The complex binding activation mechanism of these receptors, wherein a single common receptor must complex with a series of private receptors, makes rationally engineering and manipulating the activity of these receptors challenging. Further, the effects of any intervention operate across multiple distinct cell populations with unique responses to these cytokines as a consequence of their receptor expression. Thus, to guide further immune therapy development, new analysis methods like tensor factorization applied to biological systems are required to map the signaling landscape of this receptor family.

Background and Modeling

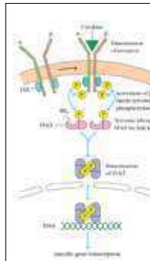

Figure 1: General model of signal transduction mediated by most Class I and Class II cytokine receptors. Binding of a cytokine induces dimerization of the receptor subunits, which leads to the activation of receptor subunit-associated JAK tyrosine kinases by reciprocal phosphorylation. Subsequently, the activated JAKs phosphorylate various tyrosine residues on the receptors, resulting in the creation of docking sites for STATs (Signal Transducers and Activators of Transcription) on the receptor and the activation of one or more STAT transcription factors. The phosphorylated STATs dimerize and translocate to the nucleus, where they activate transcription of specific genes. Since we have experimental data for p-STATS activation levels, it is important to model the surface kinetics and endosomal trafficking of the various species in order to estimate the complexes resulting in p-StatS activation.[1]

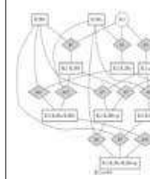

Figure 2: Complex binding activation mechanism for IL2 receptors. To model the binding behavior for IL2, IL15, IL7, and IL9, we use ordinary differential equations (total of 52) incorporating the binding and unbinding behaviors for each receptor complex. As seen in this figure, forward rate constants (k1-k12 fwd) and reverse rate constants (k1-k12 rev) need to be known in order to obtain concentration values for these receptor complexes after cytokine stimulation at various timepoints. By searching the literature for these parameter values, we narrowed 32 rate constants down to 11. We employ machine learning techniques in order to fit the model to experimental data and obtain the remaining unknowns.

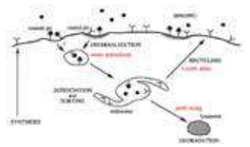

Figure 3: Endosomal receptor trafficking. Receptors mediate the selective transport of ligand from the extracellular environment to the interior of the cell. Receptor and ligand molecules may be sorted intracellularly within endosomes, governing recycling to the cell surface and delivery to lysosomes. The parameters shown in red also need to be determined through the fitting process, along with the synthesis expression rates for the receptors IL2Rα, IL2Rb, IL15Rα, IL7Rα, IL9R, and gc. Note that the gamma chain receptor (gc) is common between all four interleukins, and the IL2Rb receptor is shared between IL2 and IL15.[2]

Materials and Methods: MCMC & Tensor Factorization

Since our model incorporates the surface kinetics and endosomal trafficking of the various receptor complexes, to estimate the amount of p-STAT5, we identified 6 active compounds:

-IL2_IL2Rb_gc and IL2_IL2Rα_IL2Rb_gc for IL2
-IL15_IL2Rb_gc and IL15_IL15Rα_IL2Rb_gc for IL15
-IL7Rα_gc_IL7 for IL7
-IL9R_gc_IL9 for IL9

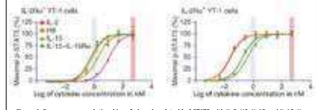

Figure 4: Dose-response relationships of phosphorylated (p-) STAT5 with IL-2, N9, IL-15 and IL-15-IL-15Rα complexes in IL-2Rα– YT cells (left) and IL-2Rα+ YT cells (right).[3]

By using machine learning packages such as scikit-learn and PyMC3, we employ probabilistic programming and Bayesian inferencing such as Markov Chain Monte Carlo (MCMC) to fit the model to the data shown in Figure 4 and obtain the remaining unknown parameters.

MCMC

Tensor Factorization

Because distinct cell lines express receptors differently and respond uniquely to varying cytokine stimulation, we need to be able to represent higher dimensional data that integrates these different cell populations' responses to various interleukins at multiple timepoints. This dimensional representation is done through tensors, which are higher order extensions of matrices showing more than just 2 dimensions.

Figure 5: Figure showing generated tensor. One dimension shows the different combinations of ligand concentrations (IL-2, IL-15, IL-7, IL-9) and receptor expression rates (IL2Rα, IL2Rb, gc, IL15Rα, IL7Rα, IL9R). The second dimension includes 1000 timepoints during which the experiments will be simulated for. The third dimension involves 16 values which we want to keep track of, which are ligand activity (IL-2, IL-15, IL-7, IL-9), surface receptor amount (IL2Rα, IL2Rb, gc, IL15Rα, IL7Rα, IL9R), and total receptor amount (IL2Rα, IL2Rb, gc, IL15Rα, IL7Rα, IL9R).

In order to achieve intuitive representation and handling of this tensor without losing the structural characteristics of the data itself, a data compression technique known as Tensor Factorization was performed.

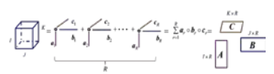

Figure 6: Canonical Polyadic Decomposition (also known as CP or PARAFAC). This decomposition follows the scheme that just as a matrix can be expressed as the sum of the outer product of two vectors, a tensor of order 3 can be expressed as the sum of the 'R' outer product of three vectors.

Results and Discussions

To decompose and explain 90% of the variance in the original tensor (X), we determined R = 8 components after comparing the R^2X metric and decomposing X using different values for R and then reconstructing it (Xr):

$R^2X = 1 - \frac{var(X_r - X)}{var(X)}$, where 'var' computes the variance.

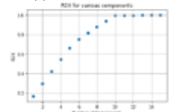

Figure 7: R^2X for various decompositions performed under different R values. It takes 8 components to explain 90% of the variance.

Figure 8: Figure showing the three factor matrices obtained from PARAFAC decomposition. Given the two dimensional structure of these factor matrices, it becomes easier to visualize trivial and nontrivial relationships within the data.

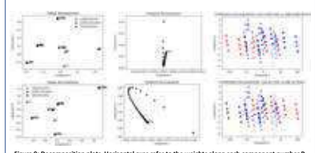

Figure 9: Decomposition plots. Horizontal axes refer to the weights along each component number R.

By studying the position of each value along the different components, we can further analyze both trivial and nontrivial relationships. For example, take IL2Rb (top right of Fig. 9), by increasing receptor expression rate (red to blue), we increase along component 1, and by multiplying it with the respective positions in the timepoint and values plots, we get that surface and total IL2Rb values increase, which is what we expect (trivial).

Conclusions

By utilizing computational modeling on both ligand-receptor interactions and endosomal receptor trafficking, we can study each ligand's effects on receptor activation. After fitting the model to experimental measurements, we computationally solve the input-output behavior of cytokine response. We finally visualize the effect cytokine stimulation has across individual immune cell populations using tensor factorization. This map of the signaling landscape for this receptor family will guide further immune therapy development.

For future avenues, we should see if we can find particular combinations of receptors that are expressed in different cell populations. Not all combinations may be biologically meaningful.

References & Acknowledgments

I would like to thank Aaron Meyer and the UCLA Bioengineering Department for mentoring and providing me with the opportunity to contribute to this work.

1. Owen JA, Punt J, Stranford SA, Jones PP. Receptors and Signaling: Cytokines and Chemokines. Kuby Immunol. 2013:110.
2. Lauffenburger, Douglas A, and Jennifer J. Linderman. Receptors: Models for Binding, Trafficking, and Signaling. New York: Oxford University Press, 1993. Print.
3. Ring AM, Lin J-X, Feng D, et al. Mechanistic and structural insight into the functional dichotomy between IL-2 and IL-15. Nat Immunol. 2012;13(12):1187–1195. doi:10.1038/ni.2449.

LAB NAME

Simonetti Research Group

FACULTY ADVISOR

Dante Simonetti

DAILY LAB SUPERVISOR

Faisal Alshafei

DEPARTMENT

Chemical amd Biomolecular Engineering

Richa Ghosh

Chemical Engineering

Sophomore

Synthesis of Mixed-Oxide Sorbents for Room-Temperature Removal of Hydrogen Sulfide

Sulfur compounds, such as hydrogen sulfide (H2S), which are present and produced in refinery streams as well as in coal- and biomass-derived processes, are environmentally toxic due to their conversion to sulfur oxides (SOx) upon combustion. The removal of these compounds is of paramount importance to industry as even trace amounts can corrode pipelines and storage tanks, poison catalysts, and impact fuel quality. Due to the chemical affinity of H2S for metallic cations, a frequently used technique for removing H2S involves reacting it over solid surfaces comprising of Zn, Fe, Ca, Mn and/or V oxide at elevated temperatures (T>523 K). However, owing to practical and economic reasons, recently there has been a growing need for the development of sorbents that are able to purify natural gas at reduced temperatures.

In this work, we investigated the synthesis of mixed oxides comprising of Cu and another metal (Zn, Al, Co, Ni, Mn, Mg, Bi, or La) using various synthetic techniques such as, electrospinning, sol-gel, and co-precipitation. By infusing a metal into the CuO structure, we sought to understand the effects of composition on morphology, thermal stability, and thermodynamic favorability of the sulfidation reaction at room temperature. Several characterization techniques were employed to elucidate information regarding structure-function relationships such as, X-ray diffraction (XRD), thermogravimetric analysis (TGA), and scanning electron microscopy (SEM).

Synthesis of Mixed-Oxide Sorbents for Room-Temperature Removal of Hydrogen Sulfide

Richa Ghosh, Akash Biswas, Faisal Alshafei, Sara Azzam and Dante Simonetti

Chemical and Biomolecular Engineering Department, University of California, Los Angeles

Introduction

- Sulfur compounds, such as hydrogen sulfide (H_2S), carbonyl sulfides and thiophenes, in hydrocarbon streams are environmentally toxic due to their conversion to sulfur oxides (SO_x) upon combustion. SO_x emissions reduce the efficiency of catalytic converters in automobiles and contribute to acid rain. In addition, sulfur compounds damage processing equipment and affect product quality.
- Copper Oxide (CuO) is an attractive sorbent for the removal of H_2S because its reaction is thermodynamically favored at low temperatures and sulfur is sequestered as a solid product.
- Mixed metal oxides have enhanced sorption selectivity and activity due to the creation of surface defects, which causes metal cations to be more accessible, and Bronsted acid sites, which result from charge balancing cations.
- In this work, various synthesis techniques were used in order to yield sorbents with different structures and physiochemical properties.

Materials Synthesis

1. Electrospinning

a. Solution Preparation

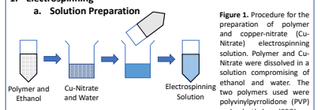

Figure 1. Procedure for the preparation of polymer and copper-nitrate (Cu-Nitrate) electrospinning solution. Polymer and Cu-Nitrate were dissolved in a solution compromising of ethanol and water. The two polymers used were polyvinylpyrrolidone (PVP) and polyethylene (PEO).

b. Electrospinning Process

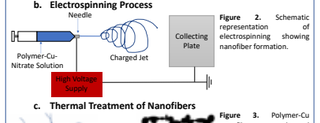

Figure 2. Schematic representation of electrospinning showing nanofiber formation.

c. Thermal Treatment of Nanofibers

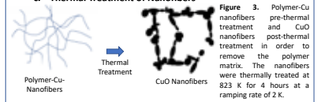

Figure 3. Polymer-Cu nanofibers pre-thermal treatment and CuO nanofibers post-thermal treatment in order to remove the polymer matrix. The nanofibers were thermally treated at 823 K for 4 hours at a ramping rate of 2 K.

2. Co-Precipitation

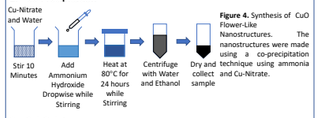

Figure 4. Synthesis of CuO Flower-Like Nanostructures. The nanostructures were made using a co-precipitation technique using ammonia and Cu-Nitrate.

3. Sol-Gel Process

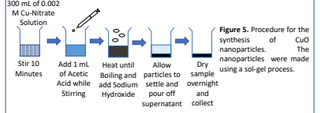

Figure 5. Procedure for the synthesis of CuO nanoparticles. The nanoparticles were made using a sol-gel process.

Reaction of H_2S and CuO

- CuO-based sorbents were packed into a fixed bed reactor and H_2S was fed into the reactor.
- $H_2S + CuO \rightarrow H_2O + CuS \quad \Delta G^{\circ}_{298} = -32.37\ \text{kcal/mol}$

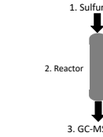

Figure 6. Diagram of fixed bed reactor. The reactor was run at a temperature of 294 K, pressure of 1 atm and had an initial H_2S concentration of 1000 ppm. In step 1 H_2S is fed through inlet streams to the reactor. In step 2 CuO sorbents are packed inside a fixed bed reactor. H_2S flows over the reactor bed and reacts with the CuO, adhering to the surface. In step 3 the GC-MS and FTIR measure sulfur pickup.

Effect of Synthesis on Pure CuO

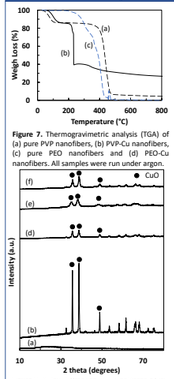

Figure 7. Thermogravimetric analysis (TGA) of (a) pure PVP nanofibers, (b) PVP-Cu nanofibers, (c) pure PEO nanofibers and (d) PEO-Cu nanofibers. All samples were run under argon.

Figure 8. X-Ray Diffraction (XRD) patterns of (a) PVP-Cu nanofibers, (b) CuO nanofibers from PVP, (c) PEO-Cu nanofibers, (d) CuO nanofibers form PEO, (e) CuO nanoparticles and (f) CuO flower-like structures. The peaks in curves (b), (d), (e) and (f) are indicative of the the planes of single-phase monoclinic CuO.

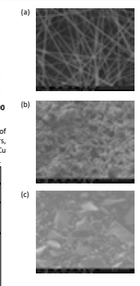

Figure 9. Scanning Electron Microscopy (SEM) images of (a) Polymer-Cu nanofibers pre-thermal treatment, (b) CuO nanofibers post-thermal treatment, (c) CuO nanoparticles and (d) CuO flower-like structures.

	Synthesis Technique		
	Electrospinning	Co-Precipitation	Sol-Gel
Surface Area (m^2/g)			
Pore Size (nm)			

Table 1. Properties of CuO sorbents. Braunauer-Emmett-Teller (BET) Analysis was used to determine the properties.

	CuO Sorbent			
	Nanofibers from PVP	Nanofibers from PEO	Nanoparticles	Flowerlike Nanostructures
k (1/s)	8.00E-03	6.96E-04	1.40E-04	3.30E-04
qs (g H_2S /100 g CuO)	0.5	2.2	12.5	7.2
Conversion %	1.19	5.24	29.76	17.14

Table 2. CuO sorbent properties.

Reaction of Pure CuO and H_2S

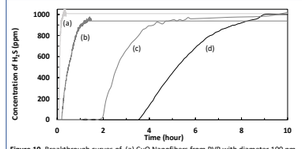

Figure 10. Breakthrough curves of (a) CuO Nanofibers from PVP with diameter 100 nm, (b) CuO Nanofibers from PEO, (c) CuO flower-like nanostructures and (d) CuO nanoparticles.

- All of the CuO sorbents were able to pick up sulfur, but at different capacities.
- As the average crystallite size of the sorbent decreased, the active pick up time increased.
- As the purity of the sorbent increased, the active pick up time increased.
- Although all of the sorbents were able to pick up sulfur, their sorption activity was limited due to the thermodynamic properties of the reaction between CuO and H_2S at room temperature . By synthesizing the CuO as a mixed metal oxide, the thermodynamic barrier of the reaction is lowered, leading to increased sorption capacity.

Effect of Metal Composition

- Mixed metal oxides were made with the metals Zn, Al and La using the sol-gel process. Ratios of 99% Cu – 1% Metal and 90% Cu – 10% Metal were made.

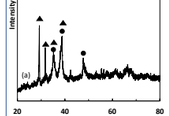

Figure 11. XRD patterns of (a) 99% Cu – 1% Zn Oxide, (b) 90% Cu – 10% Zn Oxide, (c) 99% Cu – 1% La Oxide, (d) 90% Cu – 10% La Oxide, (e) 99% Cu – 1% Ni Oxide and (f) 90% Cu – 10% Ni Oxide.

Figure 12. SEM images of (a) Cu-Zn mixed metal oxide, (b) Cu-La mixed metal oxide and (c) Cu-Ni mixed metal oxide.

	Crystallite Size (nm)	
Metal	1%	10%
Zn		
La		
Ni		

Table 3. Properties of mixed metal CuOs.

Conclusions and Future Works

- Crystallite size and purity of the sorbent sample were found to be the two main factors that contributed to increased sulfur sorption.
- Further work will involve testing different compositions of the mixed metal oxides made in this work as well as testing more metals.

Contact

Dante Simonetti
Chemical and Biomolecular Engineering Department,
University of California, Los Angeles
Email: dasimonetti@ucla.edu
Phone: 310-267-0169

References

1. Acton, Q. (Ed.). (2013). *Sulfur Compounds—Advances in Research and Application* (2013 ed.). Atlanta , GA: ScholarlyEditions., 576-579
2. Sansregret, J. L. (1980). Reaction of Copper Oxide with H_2S. *Journal of the Electrochemical Society*, 2083-2084.

Acknowledgements

Thank you to Dr. Dante Simonetti for the opportunity to work on this project, Faisal Alshafei for guidance and assistance with SEM, Sara Azzam for assistance with running the reactor and XRD, Derrick Rosales for assistance with the TGA and Zubin Mishra for assistance in electrospinning. Thank you to the Henry Samueli School of Engineering and Applied Sciences, Office of Equity, Diversity, and Inclusion at UCLA, and donors of the American Chemical Society Petroleum Research Fund for financial support of this research. Thank you to the Molecular & Nano Archaeology (MNA) Laboratory at UCLA Materials Science Department for use of the SEM, the J.D. McCullough Laboratory of X-ray Crystallography at UCLA Chemistry Department for use of the XRD, and the California NanoSystems Institute (CNSI) at UCLA for use of the TGA.

LAB NAME
Kasko Lab

FACULTY ADVISOR
Andrea Kasko

DAILY LAB SUPERVISOR
Sam Norris

DEPARTMENT
Bioengineering

Amy Guo

Bioengineering

Junior

Synthesis of Well-Defined Structural Derivatives of Glucose-Based Glycopolymers for Pentobra Potentiation Studies

It has previously been shown that metabolites such as D-glucose are able to potentiate the antibiotic activity of aminoglycosides by interfering selectively with bacterial ribosomal activity, thereby eradicating bacterial persisters. Pentobra, a membrane-active aminoglycoside-peptide conjugate (MAAPC), combines the ribosomal-related function of aminoglycosides with the bacterial membrane-disrupting aspect of polypeptides for a 4-6 log increase in bactericidal activity over free tobramycin. We hypothesize that Pentobra will similarly be potentiated by D-glucose containing macromolecules. Use of the macromolecular saccharide chain instead of small molecules (i.e. glucose) in potentiation allows for direct conjugation of the glycopolymer to Pentobra, producing a single-molecule antibiotic with multiple synergistic aspects. However, it is also currently unclear what polymer architecture would best potentiate Pentobra, and the processes of glucose-release/bacterial uptake of the glycopolymer are not yet fully understood. To address these issues, we have used reversible addition-fragmentation chain-transfer (RAFT) polymerization to synthesize several well-defined glucose-based glycopolymers of varying backbone connectivity and chain length for further antibiotic potentiation studies. A better understanding of the potentiation mechanism and in turn the relationship between glycopolymer structure and potentiation will hopefully lead to a new alternative to treat antibiotic-resistant infections.

Synthesis of Well-Defined Structural Derivatives of Glucose-Based Glycopolymers for Antibiotic Potentiation Studies

Amy B. Guo[1], Walter T. Liau[1], Andrea M. Kasko[1]
[1]UCLA Department of Bioengineering

Background

- Glucose potentiates aminoglycosides and enables eradication of bacterial persisters
- Pentobra is a membrane-active aminoglycoside-peptide conjugate that has a 4-6 log increase in bactericidal activity compared to tobramycin (an aminoglycoside)

Structure and function of Pentobra. The aminoglycoside (yellow) structure allows Pentobra to target bacterial ribosomes while the short peptide sequence (blue) allows for selective disruption of bacterial membranes.

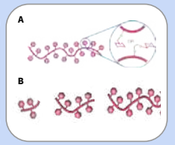

Polymer architecture. (A) Backbone connectivity and (B) chain length (or degree of polymerization) variants of glucose-based glycopolymers were synthesized via RAFT polymerization for future antibiotic potentiation studies.

HYPOTHESIS A glucose-based glycopolymer will also potentiate Pentobra, and the structure of the glycopolymer will affect bactericidal activity.
APPROACH A glucose-based glycopolymer was co-delivered with Pentobra to E. coli persisters. Two protected glucose-based glycopolymers that present glucose with either C-1 or C-6 backbone connectivity, each of varying chain length, were synthesized via RAFT for future potentiation studies.

Materials and Methods

SCHEME 1: Synthesis of acetate-protected glycomonomers. Synthesis of (A) 2-O-(2,3,4,6- Tetraacetyl-β-D-glucosyl)hydroxyethyl acrylate and (B) methacryloyl-1,2,3,4-tetraacetate-β-D-glucose from D-glucose.

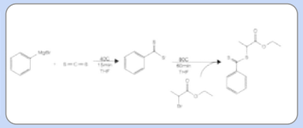

SCHEME 2: Synthesis of ethyl 2-(phenylcarbonothioylthio) propionate. The RAFT CTA agent was synthesized from phenylmagnesium bromide, carbon disulfide, and ethyl 2-bromopropionate.

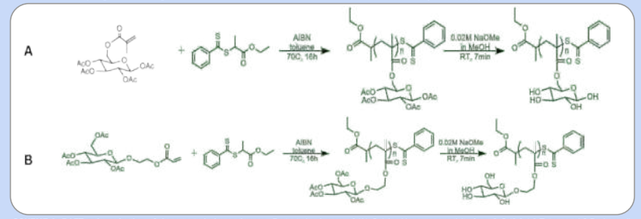

SCHEME 3: RAFT polymerization of deprotected glycopolymers. Protected polymers of (A) C-1 backbone connectivity from 2-O-(2,3,4,6-Tetraacetyl-β-D-glucosyl) hydroxyethyl acrylate monomer and (B) C-6 backbone connectivity from 6-methacryloyl-1,2,3,4-tetraacetate-β-D-glucose monomer were synthesized via RAFT using ethyl 2-(phenylcarbonothioylthio) propionate as the chain transfer agent (CTA) and azobisisobutyronitrile (AIBN) as the thermoinitator at 70C for 16h. Deprotection will be done using 0.02M NaOMe in MeOH at room temperature (RT) for 7min.

Results

RAFT polymerization inhibiting impurity

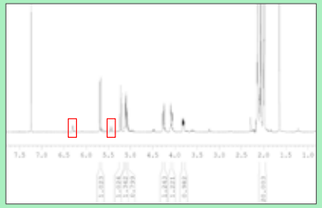

Impurity during synthesis of 1,2,3,4,6-pentaacetyl-β-D-glucose. ^{1}H NMR of 1,2,3,4,6-pentaacetyl- β-D-glucose in $CDCl_3$ showing impurity peaks at δ6.30(d) and 5.44(t). Heating reaction to 140°C in presence of O_2 produced impurity that interacted with the RAFT CTA, inhibiting RAFT polymerization of methyl acrylate at 10 mol%. Avoid formation during synthesis of monomer by purging reaction vessel and solvent with inert gas and reducing heat to 100°C.

Glycopolymer characterization

Monomer	2-O-(2,3,4,6-Tetraacetyl-β-D-glucosyl)hydroxyethyl acrylate			Methacryloyl-1,2,3,4-tetraacetate-β-D-glucose		
Target DP	25	50	100	25	50	100
DP[a]	22	38	63	13	39	47
DP[b]	13	23	38			
Polydispersity[b]	1.0698	1.2745	1.0724			
Degree of Conversion (%)[a]	96	85	75	92	90	83

Glycopolymer chain length and degree of conversion. The degree of polymerization was less than the target value for all glycopolymers by ^{1}H NMR. The degree of conversion for all polymers were in relatively high yield.
[a] calculated by ^{1}H NMR in $CDCl_3$
[b] calculated by GPC in THF calibrated with linear polystyrene standards

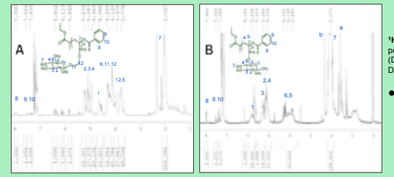

^{1}H NMR spectral data of protected glycopolymers. ^{1}H NMR of (A) poly(2-O-(2,3,4,6-Tetraacetyl-β-D-glucosyl)hydroxyethyl acrylate) (DP≈25) and (B) poly (6-methacryloyl-1,2,3,4-tetraacetate-β-D-glucose) (DP≈25) crude RAFT polymerization reaction in $CDCl_3$.

- ^{1}H NMR indicates both reactions went mostly to completion and had DP values slightly lower than the target number (see glycopolymer characterization data)

Pentobra potentiation by poly(6-acryloyl-D-glucose)

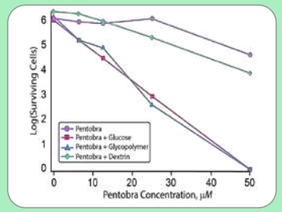

Pentobra is potentiated by the glycopolymer poly(6-acryloyl-D-glucose). Pentobra was administered to *E. coli* bacterial persisters without any glucose-containing compound, with the monosaccharide D-glucose, with poly(6-acryloyl-D-glucose) DP=14, and with dextrin (hydrolyzed starch that can be metabolized to D-glucose). All glucose-containing compounds were present at a glucose-repeat unit concentration of 0.7mM. While dextrin was unable to potentiate antibiotic activity, both the monosaccharide and glucose-containing glycopolymer were able to increase the bactericidal activity of Pentobra by up to 4 log. The potentiation appears to be synergistic rather than additive.

Conclusions

- Pentobra is potentiated by co-delivery with a glucose-based glycopolymer
- Protected glucose-based glycopolymers have been synthesized of three distinct degrees of polymerization and two backbone connectivities (C-1 vs. C-6) with appreciable degrees of conversion

Future Directions

Glycopolymer organic synthesis
- Deprotection of acetate groups for all synthetic glycopolymers

Antibiotic potentiation studies
- Co-deliver deprotected glycopolymers with Pentobra to E. coli bacterial persisters and observe differences in bactericidal activity

Acknowledgements
Thank you to Walter T. Liau for obtaining the data in *Pentobra potentiation by poly(6-acryloyl-D-glucose)*. This project is possible with funding from the National Institutes of Health, the National Science Foundation, ...

Yuwan Guo

Chemical Engineering

Junior

LAB NAME

Monbouquette Laboratory

FACULTY ADVISOR

Harold Monbouquette

DAILY LAB SUPERVISOR

Brenda Huang

DEPARTMENT

Chemical and Biomolecular Engineering

Model-Guided Optimization of Electroenzymatic Biosensors for Neurotransmitter, Glutamate

Neurotransmitters are critical in regulating processes such as mental performance, emotions, and pain response. Researchers have found that neurotransmitters, for example, glutamate, is associated with depression and bipolar disorder. Moreover, altered glutamatergic neurotransmission appears to be central to the pathophysiology of Parkinson's disease. Therefore, monitoring glutamate activities in the brain can illuminate the mechanisms behind and the progression of neurological diseases and disorders. Electroenzymatic biosensors can provide improved temporal and spatial resolutions for measuring glutamate concentration change in the brain. Because of the non-electroactive nature of glutamate, direct electrochemical methods cannot be used. However, electroenzymatic approaches to biosensor design, incorporating permselective layer to block out electroactive interferences and utilizing glutamate oxidase (GlutOx) as the biochemical recognition element, can be developed and optimized. In the presence of oxygen, GlutOx produces hydrogen peroxide (H_2O_2), which passes through the permselective layer and is electrooxidized at the electrode surface, generating a recordable current signal that allows for glutamate detection.

Biosensor performances can be simulated using a detailed mathematical model to predict the modification of sensor designs. The mathematical simulation has suggested that thinner permselective layer and thinner enzyme layer generate faster sensor response time and higher sensitivity. Based on the simulation, permselective layer thickness and enzyme layer thickness of biosensors for monitoring glutamate activity are optimized and the sensitivity is improved six fold to 290±14 nA/μM/cm² and the response time is decreased to <0.4s.

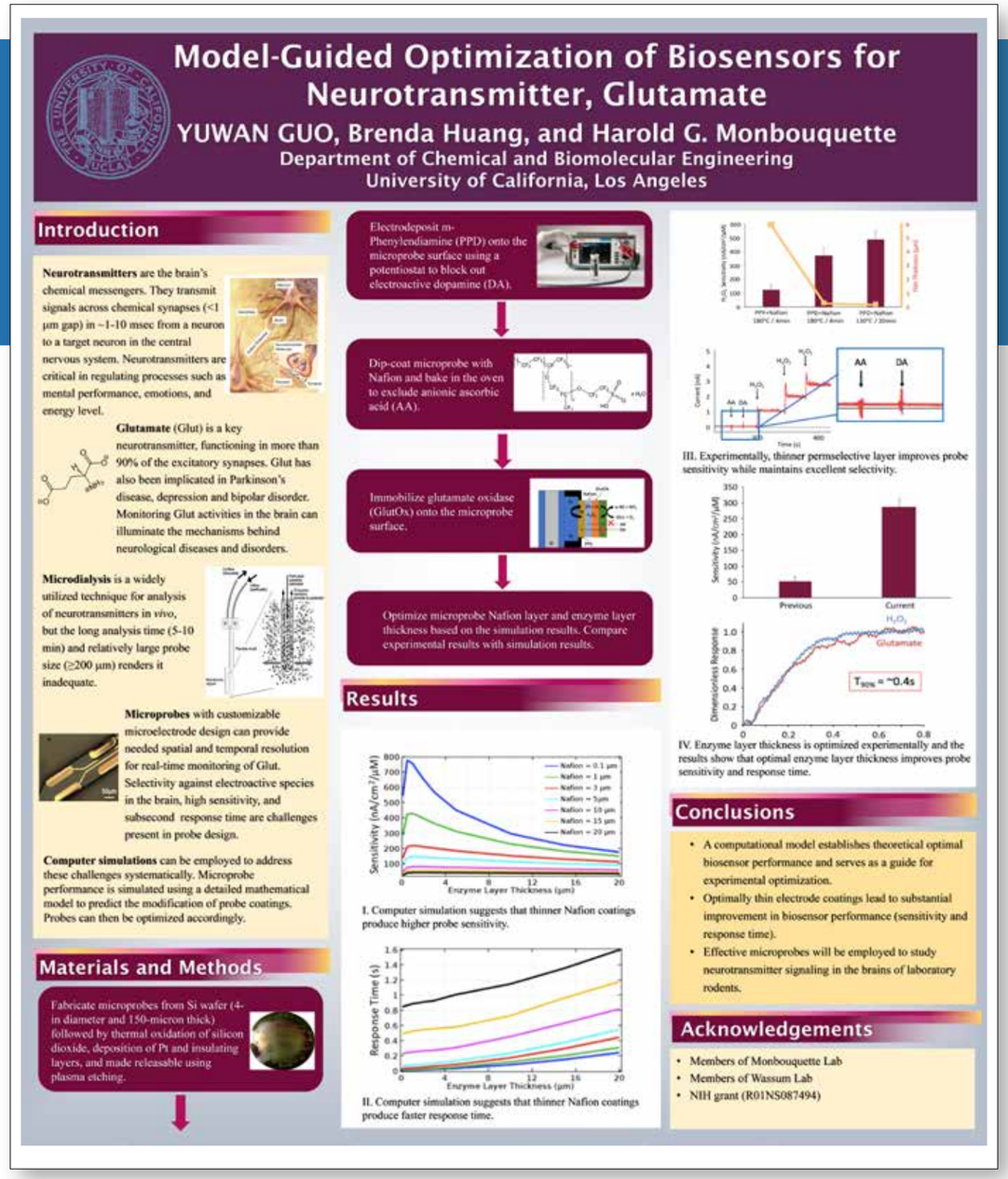

Jacob Hambalek

Bioengineering

Junior

LAB NAME

Di Carlo Laboratory

FACULTY ADVISOR

Dino Di Carlo

DAILY LAB SUPERVISOR

Janay Kong and Kahlen Ouyang

DEPARTMENT

Bioengineering

A Quantitative Rapid Nucleic Acid Methylation Assay Using Loop Mediated Isothermal Amplification

Nucleic acid methylation has become increasingly noteworthy in recent years, regarded as an epigenetic indicator of gene regulation. Current technology for detection of methylated nucleic acids is limited to assays that are time consuming and/or require equipment that is expensive and bulky. We have developed a quantitative and rapid nucleic acid methylation detection assay, which utilizes methylation sensitive restriction enzymes and a unique amplification method, known as Loop Mediated Isothermal Amplification (LAMP). This new technology is far more rapid than current methylation detection methods, and does not require highly specialized and expensive laboratory benchtop equipment. The unique mechanism of LAMP ensures that amplification is significantly hindered when the locus of amplification is cut by restriction enzymes. Methylation sensitive restriction enzymes do not perform their function, cutting DNA strands at a specific site, when their target site includes a methylated base. The use of FastDigest restriction enzymes, in which the digestion process is significantly quicker than that of traditional restriction enzymes, contributes to a rapid total assay time much less than that of the current methylation detections assays available. Methylation of the DNA target with CpG Methyltransferase allows for controlled proof-of-concept analysis of the assay on methylated DNA. Further realization of specific genomic sites and downstream misregulation of proteins will lead to the selection of multiple target sequences to be tested as indicators of disease susceptibility. Future applications include the development of a mobile clinic device capable of providing lifesaving diagnostics for underserved communities.

A Quantitative Rapid Nucleic Acid Methylation Detection Assay

Jacob Hambalek[1,4], Janay Kong[1], Dino Di Carlo[1,2,3]

1. Department of Bioengineering, University of California Los Angeles, Los Angeles, CA, USA; 2. California NanoSystems Institute, UCLA; 3. Jonsson Comprehensive Cancer Center, UCLA; 4. Undergraduate Research Program, UCLA Samueli School of Engineering and Applied Science

Methylation and Epigenetics

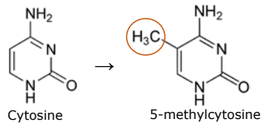

- Responsible in part for gene regulation
- Mechanism of Aging
- Only occurs at CpG dinucleotide in mammalian genome

- Can occur at genomic sites that lead to downstream abnormalities:
  - Repression of structural proteins (Cardiovascular Disease)
  - Unregulated proliferation (Cancer)

Loop Mediated Isothermal Amplification

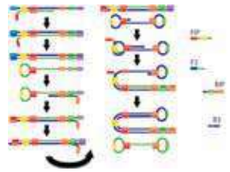

- Inner and outer primers on both 5′ and 3′ end create dumbbell structure
- Dumbbell structure mediates multiple sites for primer annealing
- Amplified product completely folds over itself
  - Complement forms new dumbbell structure for further amplification

Methylation Sensitive Restriction Enzymes

- Restriction enzymes cleave DNA at specific recognition sites.
- When these sites are methylated, methylation sensitive restriction enzymes **do not cleave**

HpyCH4IV	SsiI
5′ … A||CGT … 3′	5′ … C||CGC … 3′
3′ … TGC||A … 5′	3′ … GGC||G … 5′

The methylation sensitive enzymes chosen for this assay were independently selected based on the following criteria:

1. Restriction Site Contains CpG **2.** Fast Digest Protocols (5-15 min)
3. Heat Inactivated

Materials and Methods

- Incubation of Lambda DNA target with CpG Methyltransferase adds methyl group to CpG sites for **controlled methylation analysis**
- Cleavage of unmethylated DNA target by enzymes and validation of methylated DNA resistance to cleavage confirmed through Gel Electrophoresis

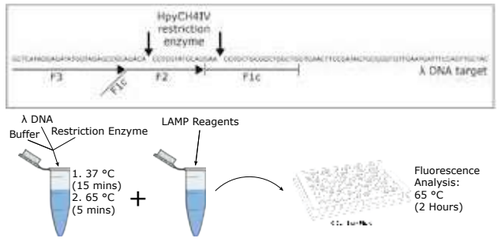

Results

Uniqueness of LAMP in Methylation Detection

- Dumbbell conformations disabled when strand is cleaved by enzyme
- Real time fluorescence measurement indicates amplification is significantly hindered

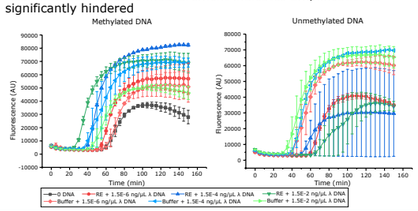

Conclusion

First methylation detection assay applicable for point of care setting

- Rapid
- Isothermal
- Quantitative

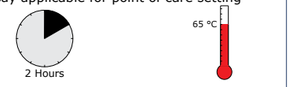

Applications

Clinically Relevant Genomic DNA Targets

- Genes that, when under or over methylated, are linked to:

Atherosclerosis

http://www.emdmillipore.com/US/en/product/CpGenome-Universal-Unmethylated-DNA,MM_NF-S7822?ReferrerURL=https%3A%2F%2Fwww.google.com%2F

Atherosclerosis – Medical News Bulletin | Health News and Medical Research, 2017

Other life-threatening diseases

- Cancer
- Autoimmune Diseases

Mobile Fluorescence Readout

- Efficacious: Greater stability and sensitivity achieved through intercalating and sequestering dye combination
- Accessible: Significantly cheaper than benchtop plate readers
- Mobile: Can be taken to resource poor areas for diagnostic testing

References

Tsugunori Notomi, et al; Loop-mediated isothermal amplification of DNA, *Nucleic Acids Research*, Volume 28, Issue 12, 15 June 2000

Dino Di Carlo, Janay E. Kong, Aydogan Ozcan, Omai Garner; Enhanced fluorescence readout and reduced inhibition for nucleic acid amplification tests; WO2017201060A1

Janay E. Kong, et al; Highly Stable and Sensitive Nucleic Acid Amplification and Cell-Phone-Based Readout, *ACS Nano* 2017 *11* (3), 2934-2943

Funding & Acknowledgments

Di Carlo Microfluidics Laboratory
Kahlen Ouyang
UCLA Samueli Engineering Undergraduate Research Program
National Science Foundation Engineering Research Centers: PATHS UP

Thomas Horn

Bioengineering

Junior

LAB NAME

Di Carlo Laboratory

FACULTY ADVISOR

Dino Di Carlo

DAILY LAB SUPERVISOR

Jaekyung Koh

DEPARTMENT

Bioengineering

Transport and Release of Model Antigen and Adjuvant Species in a Hydrogel Cancer Vaccine

Cancer vaccination is a therapeutic method that applies the immune system to destroy cancer cells. This approach relies on releasing antigen (tumor-specific molecule) and appropriate adjuvants (substances that activate cells of the immune system) into the body with spatial and temporal control. Previous research in the field has demonstrated that cationic particles for vaccine delivery increase cellular response to cancer vaccines. Di Carlo et al.'s MAP (microporous annealed particle) hydrogel system is highly biocompatible and has tunable chemistry, enabling a wide variety of modifications, including the addition of cationic functionalities. As part of developing MAP for cancer vaccination, this research project will determine the loading and release of antigens and adjuvants induced by a variety of loading methods. Firstly, it was verified that molecules incorporated into the hydrogel could be released by diffusion. FRAP (fluorescence recovery after photobleaching) was used to measure diffusivity of adjuvant-sized (fluorescein) and antigen-sized (70kDa dextran-FITC) molecules in the hydrogel. Secondly, the maximum concentrations of protein antigen (ovalbumin) loaded onto MAP by diffusion and encapsulation were determined by BCA (bicinchoninic acid) assay and fluorescence. Finally, the released concentrations of antigen and adjuvant for MAP loaded by diffusion and fluorescence were determined by incubating the loaded gels in release media and withdrawing samples for fluorescence tests. The diffusivities of high and low-molecular weight species in the MAP system did not change significantly with composition, suggesting that diffusive transport considerations need not limit the choice of MAP formulation for a cancer vaccine application.

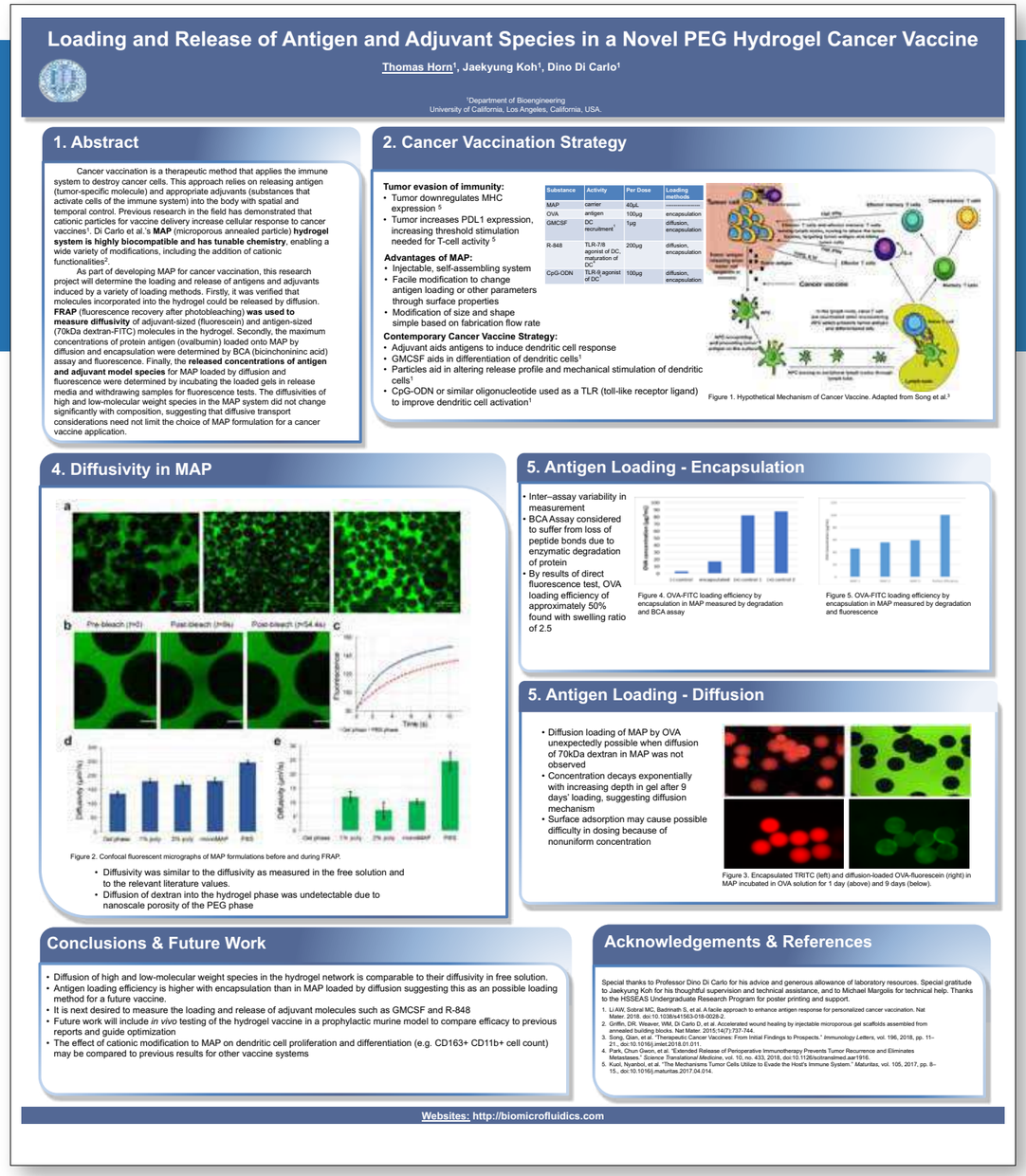

Loading and Release of Antigen and Adjuvant Species in a Novel PEG Hydrogel Cancer Vaccine

Thomas Horn[1], Jaekyung Koh[1], Dino Di Carlo[1]

[1]Department of Bioengineering
University of California, Los Angeles, California, USA.

1. Abstract

Cancer vaccination is a therapeutic method that applies the immune system to destroy cancer cells. This approach relies on releasing antigen (tumor-specific molecule) and appropriate adjuvants (substances that activate cells of the immune system) into the body with spatial and temporal control. Previous research in the field has demonstrated that cationic particles for vaccine delivery increase cellular response to cancer vaccines[1]. Di Carlo et al.'s **MAP** (microporous annealed particle) **hydrogel system is highly biocompatible and has tunable chemistry**, enabling a wide variety of modifications, including the addition of cationic functionalities[2].

As part of developing MAP for cancer vaccination, this research project will determine the loading and release of antigens and adjuvants induced by a variety of loading methods. Firstly, it was verified that molecules incorporated into the hydrogel could be released by diffusion. **FRAP** (fluorescence recovery after photobleaching) **was used to measure diffusivity** of adjuvant-sized (fluorescein) and antigen-sized (70kDa dextran-FITC) molecules in the hydrogel. Secondly, the maximum concentrations of protein antigen (ovalbumin) loaded onto MAP by diffusion and encapsulation were determined by BCA (bicinchoninic acid) assay and fluorescence. Finally, the **released concentrations of antigen and adjuvant model species** for MAP loaded by diffusion and fluorescence were determined by incubating the loaded gels in release media and withdrawing samples for fluorescence tests. The diffusivities of high and low-molecular weight species in the MAP system did not change significantly with composition, suggesting that diffusive transport considerations need not limit the choice of MAP formulation for a cancer vaccine application.

2. Cancer Vaccination Strategy

Tumor evasion of immunity:
- Tumor downregulates MHC expression [5]
- Tumor increases PDL1 expression, increasing threshold stimulation needed for T-cell activity [5]

Advantages of MAP:
- Injectable, self-assembling system
- Facile modification to change antigen loading or other parameters through surface properties
- Modification of size and shape simple based on fabrication flow rate

Contemporary Cancer Vaccine Strategy:
- Adjuvant aids antigens to induce dendritic cell response
- GMCSF aids in differentiation of dendritic cells[1]
- Particles aid in altering release profile and mechanical stimulation of dendritic cells[1]
- CpG-ODN or similar oligonucleotide used as a TLR (toll-like receptor ligand) to improve dendritic cell activation[1]

Substance	Activity	Per Dose	Loading methods
MAP	carrier	40µL	----------
OVA	antigen	100µg	encapsulation
GMCSF	DC recruitment[1]	1µg	diffusion, encapsulation
R-848	TLR-7/8 agonist of DC, maturation of DC	200µg	diffusion, encapsulation
CpG-ODN	TLR-9 agonist of DC	100µg	diffusion, encapsulation

Figure 1. Hypothetical Mechanism of Cancer Vaccine. Adapted from Song et al.[3]

4. Diffusivity in MAP

Figure 2. Confocal fluorescent micrographs of MAP formulations before and during FRAP.

- Diffusivity was similar to the diffusivity as measured in the free solution and to the relevant literature values.
- Diffusion of dextran into the hydrogel phase was undetectable due to nanoscale porosity of the PEG phase

5. Antigen Loading - Encapsulation

- Inter–assay variability in measurement
- BCA Assay considered to suffer from loss of peptide bonds due to enzymatic degradation of protein
- By results of direct fluorescence test, OVA loading efficiency of approximately 50% found with swelling ratio of 2.5

Figure 4. OVA-FITC loading efficiency by encapsulation in MAP measured by degradation and BCA assay

Figure 5. OVA-FITC loading efficiency by encapsulation in MAP measured by degradation and fluorescence

5. Antigen Loading - Diffusion

- Diffusion loading of MAP by OVA unexpectedly possible when diffusion of 70kDa dextran in MAP was not observed
- Concentration decays exponentially with increasing depth in gel after 9 days' loading, suggesting diffusion mechanism
- Surface adsorption may cause possible difficulty in dosing because of nonuniform concentration

Figure 3. Encapsulated TRITC (left) and diffusion-loaded OVA-fluorescein (right) in MAP incubated in OVA solution for 1 day (above) and 9 days (below).

Conclusions & Future Work

- Diffusion of high and low-molecular weight species in the hydrogel network is comparable to their diffusivity in free solution.
- Antigen loading efficiency is higher with encapsulation than in MAP loaded by diffusion suggesting this as an possible loading method for a future vaccine.
- It is next desired to measure the loading and release of adjuvant molecules such as GMCSF and R-848
- Future work will include *in vivo* testing of the hydrogel vaccine in a prophylactic murine model to compare efficacy to previous reports and guide optimization
- The effect of cationic modification to MAP on dendritic cell proliferation and differentiation (e.g. CD163+ CD11b+ cell count) may be compared to previous results for other vaccine systems

Acknowledgements & References

Special thanks to Professor Dino Di Carlo for his advice and generous allowance of laboratory resources. Special gratitude to Jaekyung Koh for his thoughtful supervision and technical assistance, and to Michael Margolis for technical help. Thanks to the HSSEAS Undergraduate Research Program for poster printing and support.

1. Li AW, Sobral MC, Badrinath S, et al. A facile approach to enhance antigen response for personalized cancer vaccination. Nat Mater. 2018. doi:10.1038/s41563-018-0028-2.
2. Griffin, DR, Weaver, WM, Di Carlo D, et al. Accelerated wound healing by injectable microporous gel scaffolds assembled from annealed building blocks. Nat Mater. 2015;14(7):737-744.
3. Song, Qian, et al. "Therapeutic Cancer Vaccines: From Initial Findings to Prospects." *Immunology Letters*, vol. 196, 2018, pp. 11–21., doi:10.1016/j.imlet.2018.01.011.
4. Park, Chun Geon, et al. "Extended Release of Perioperative Immunotherapy Prevents Tumor Recurrence and Eliminates Metastases." *Science Translational Medicine*, vol. 10, no. 433, 2018, doi:10.1126/scitranslmed.aar1916.
5. Kuol, Nyanbol, et al. "The Mechanisms Tumor Cells Utilize to Evade the Host's Immune System." *Maturitas*, vol. 105, 2017, pp. 8–15., doi:10.1016/j.maturitas.2017.04.014.

Websites: http://biomicrofluidics.com

Veronica Hughey

Bioengineering

Junior

LAB NAME

Tawil Lab

FACULTY ADVISOR

Nabil Tawil

DAILY LAB SUPERVISOR

Chase Linsley

DEPARTMENT

Bioengineering

Effect of Platelet Derived Growth Factor (PDGF) and Connexin Peptides on Human-Foreskin Fibroblast (HFF) Proliferation

Chronic wounds are a major problem in the healthcare industry and their prevalence continues to increase with rise in conditions such as diabetes, heart disease, and obesity that may affect the rate of wound healing. In this study, two key peptides in the wound healing process are investigated for their potential in increasing cell proliferation, making them candidates for use in wound healing research and chronic wound therapy. These peptides are a PDGF peptide thought to have an effect on cell migration as well as a connexin mimetic peptide corresponding to the Gap27 domain thought to have an effect on intercellular communication. The effect of these peptides on human foreskin fibroblasts (HFFs) was investigated using two different in vitro models: a 2D cell monolayer on polystyrene commonly used in wound healing experiments and a more realistic 3D fibrin bead model to compare the effect of these two different environments on cell behavior. Preliminary data shows that the results of increasing peptide concentration can vary depending on the type of model used. While increasing concentration of Gap27 had a positive effect on cell proliferation in the 2D model, the opposite effect was observed in the 3D model. While this study shows the promise of using short, easily synthesized peptides in place of large growth factors for wound healing purposes, it also shows that the impact of the assay type used to study cellular behavior cannot be ignored as it can have drastic effects on the data observed.

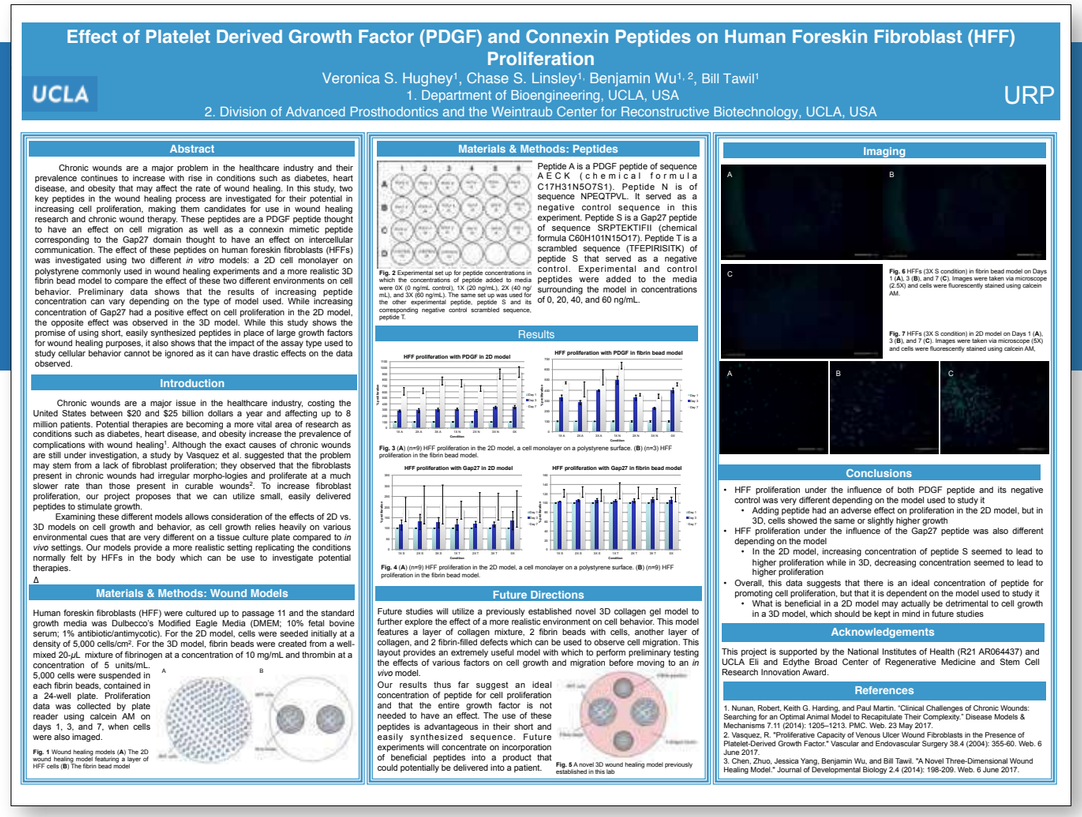

Effect of Platelet Derived Growth Factor (PDGF) and Connexin Peptides on Human Foreskin Fibroblast (HFF) Proliferation

Veronica S. Hughey[1], Chase S. Linsley[1], Benjamin Wu[1, 2], Bill Tawil[1]

1. Department of Bioengineering, UCLA, USA

2. Division of Advanced Prosthodontics and the Weintraub Center for Reconstructive Biotechnology, UCLA, USA

UCLA URP

Abstract

Chronic wounds are a major problem in the healthcare industry and their prevalence continues to increase with rise in conditions such as diabetes, heart disease, and obesity that may affect the rate of wound healing. In this study, two key peptides in the wound healing process are investigated for their potential in increasing cell proliferation, making them candidates for use in wound healing research and chronic wound therapy. These peptides are a PDGF peptide thought to have an effect on cell migration as well as a connexin mimetic peptide corresponding to the Gap27 domain thought to have an effect on intercellular communication. The effect of these peptides on human foreskin fibroblasts (HFFs) was investigated using two different *in vitro* models: a 2D cell monolayer on polystyrene commonly used in wound healing experiments and a more realistic 3D fibrin bead model to compare the effect of these two different environments on cell behavior. Preliminary data shows that the results of increasing peptide concentration can vary depending on the type of model used. While increasing concentration of Gap27 had a positive effect on cell proliferation in the 2D model, the opposite effect was observed in the 3D model. While this study shows the promise of using short, easily synthesized peptides in place of large growth factors for wound healing purposes, it also shows that the impact of the assay type used to study cellular behavior cannot be ignored as it can have drastic effects on the data observed.

Introduction

Chronic wounds are a major issue in the healthcare industry, costing the United States between $20 and $25 billion dollars a year and affecting up to 8 million patients. Potential therapies are becoming a more vital area of research as conditions such as diabetes, heart disease, and obesity increase the prevalence of complications with wound healing[1]. Although the exact causes of chronic wounds are still under investigation, a study by Vasquez et al. suggested that the problem may stem from a lack of fibroblast proliferation; they observed that the fibroblasts present in chronic wounds had irregular morpho-logies and proliferate at a much slower rate than those present in curable wounds[2]. To increase fibroblast proliferation, our project proposes that we can utilize small, easily delivered peptides to stimulate growth.

Examining these different models allows consideration of the effects of 2D vs. 3D models on cell growth and behavior, as cell growth relies heavily on various environmental cues that are very different on a tissue culture plate compared to *in vivo* settings. Our models provide a more realistic setting replicating the conditions normally felt by HFFs in the body which can be use to investigate potential therapies.

Δ

Materials & Methods: Wound Models

Human foreskin fibroblasts (HFF) were cultured up to passage 11 and the standard growth media was Dulbecco's Modified Eagle Media (DMEM; 10% fetal bovine serum; 1% antibiotic/antimycotic). For the 2D model, cells were seeded initially at a density of 5,000 cells/cm^2. For the 3D model, fibrin beads were created from a well-mixed 20-μL mixture of fibrinogen at a concentration of 10 mg/mL and thrombin at a concentration of 5 units/mL. 5,000 cells were suspended in each fibrin beads, contained in a 24-well plate. Proliferation data was collected by plate reader using calcein AM on days 1, 3, and 7, when cells were also imaged.

Fig. 1 Wound healing models (**A**) The 2D wound healing model featuring a layer of HFF cells (**B**) The fibrin bead model

Materials & Methods: Peptides

Fig. 2 Experimental set up for peptide concentrations in which the concentrations of peptide added to media were 0X (0 ng/mL control), 1X (20 ng/mL), 2X (40 ng/mL), and 3X (60 ng/mL). The same set up was used for the other experimental peptide, peptide S and its corresponding negative control scrambled sequence, peptide T.

Peptide A is a PDGF peptide of sequence AECK (chemical formula C17H31N5O7S1). Peptide N is of sequence NPEQTPVL. It served as a negative control sequence in this experiment. Peptide S is a Gap27 peptide of sequence SRPTEKTIFII (chemical formula C60H101N15O17). Peptide T is a scrambled sequence (TFEPIRISITK) of peptide S that served as a negative control. Experimental and control peptides were added to the media surrounding the model in concentrations of 0, 20, 40, and 60 ng/mL.

Results

Fig. 3 (**A**) (n=9) HFF proliferation in the 2D model, a cell monolayer on a polystyrene surface. (**B**) (n=3) HFF proliferation in the fibrin bead model.

Fig. 4 (**A**) (n=9) HFF proliferation in the 2D model, a cell monolayer on a polystyrene surface. (**B**) (n=9) HFF proliferation in the fibrin bead model.

Future Directions

Future studies will utilize a previously established novel 3D collagen gel model to further explore the effect of a more realistic environment on cell behavior. This model features a layer of collagen mixture, 2 fibrin beads with cells, another layer of collagen, and 2 fibrin-filled defects which can be used to observe cell migration. This layout provides an extremely useful model with which to perform preliminary testing the effects of various factors on cell growth and migration before moving to an *in vivo* model.

Our results thus far suggest an ideal concentration of peptide for cell proliferation and that the entire growth factor is not needed to have an effect. The use of these peptides is advantageous in their short and easily synthesized sequence. Future experiments will concentrate on incorporation of beneficial peptides into a product that could potentially be delivered into a patient.

Fig. 5 A novel 3D wound healing model previously established in this lab

Imaging

Fig. 6 HFFs (3X S condition) in fibrin bead model on Days 1 (**A**), 3 (**B**), and 7 (**C**). Images were taken via microscope (2.5X) and cells were fluorescently stained using calcein AM.

Fig. 7 HFFs (3X S condition) in 2D model on Days 1 (**A**), 3 (**B**), and 7 (**C**). Images were taken via microscope (5X) and cells were fluorescently stained using calcein AM.

Conclusions

- HFF proliferation under the influence of both PDGF peptide and its negative control was very different depending on the model used to study it
  - Adding peptide had an adverse effect on proliferation in the 2D model, but in 3D, cells showed the same or slightly higher growth
- HFF proliferation under the influence of the Gap27 peptide was also different depending on the model
  - In the 2D model, increasing concentration of peptide S seemed to lead to higher proliferation while in 3D, decreasing concentration seemed to lead to higher proliferation
- Overall, this data suggests that there is an ideal concentration of peptide for promoting cell proliferation, but that it is dependent on the model used to study it
  - What is beneficial in a 2D model may actually be detrimental to cell growth in a 3D model, which should be kept in mind in future studies

Acknowledgements

This project is supported by the National Institutes of Health (R21 AR064437) and UCLA Eli and Edythe Broad Center of Regenerative Medicine and Stem Cell Research Innovation Award.

References

1. Nunan, Robert, Keith G. Harding, and Paul Martin. "Clinical Challenges of Chronic Wounds: Searching for an Optimal Animal Model to Recapitulate Their Complexity." Disease Models & Mechanisms 7.11 (2014): 1205–1213. PMC. Web. 23 May 2017.
2. Vasquez, R. "Proliferative Capacity of Venous Ulcer Wound Fibroblasts in the Presence of Platelet-Derived Growth Factor." Vascular and Endovascular Surgery 38.4 (2004): 355-60. Web. 6 June 2017.
3. Chen, Zhuo, Jessica Yang, Benjamin Wu, and Bill Tawil. "A Novel Three-Dimensional Wound Healing Model." Journal of Developmental Biology 2.4 (2014): 198-209. Web. 6 June 2017.

Kerim Doruk Karinca

Computer Science and Engineering

Junior

LAB NAME

The Ozcan Research Group

FACULTY ADVISOR

Aydogan Ozcan

DAILY LAB SUPERVISOR

Pengbin Yin

DEPARTMENT

Electrical Engineering

Title of Research Project Title of Research Project Title of Research Project

Several investigations in biotechnology and its applications have called for a need for accurate detection and labelling of certain cell types in samples. Here we present a field-portable and cost-effective smartphone based microscope for detection and classification of Nosema ceranae, which is a honey bee parasite and causes the colony collapse disorder, through image analysis techniques.

Our portable microscope is a smartphone camera coupled with a custom developed smartphone case. The mechanical parts of the microscope are 3D printed and optical parts such as LEDs and an emission filter are mounted. We used a custom image processing algorithm to determine if and where Nosema ceranae spores are located. The algorithm is on our servers; the image is sent to our servers through the custom-made smartphone application for image processing and spore count. The result is then sent back to user over the application and displayed on the smartphone's screen.

This prototype can be used in-field to rapidly diagnose Nosema ceranae in a much shorter time compared to traditional diagnosis methods based on imaging samples using a benchtop fluorescence microscope. It can also be used by untrained technicians with minimal training alike.

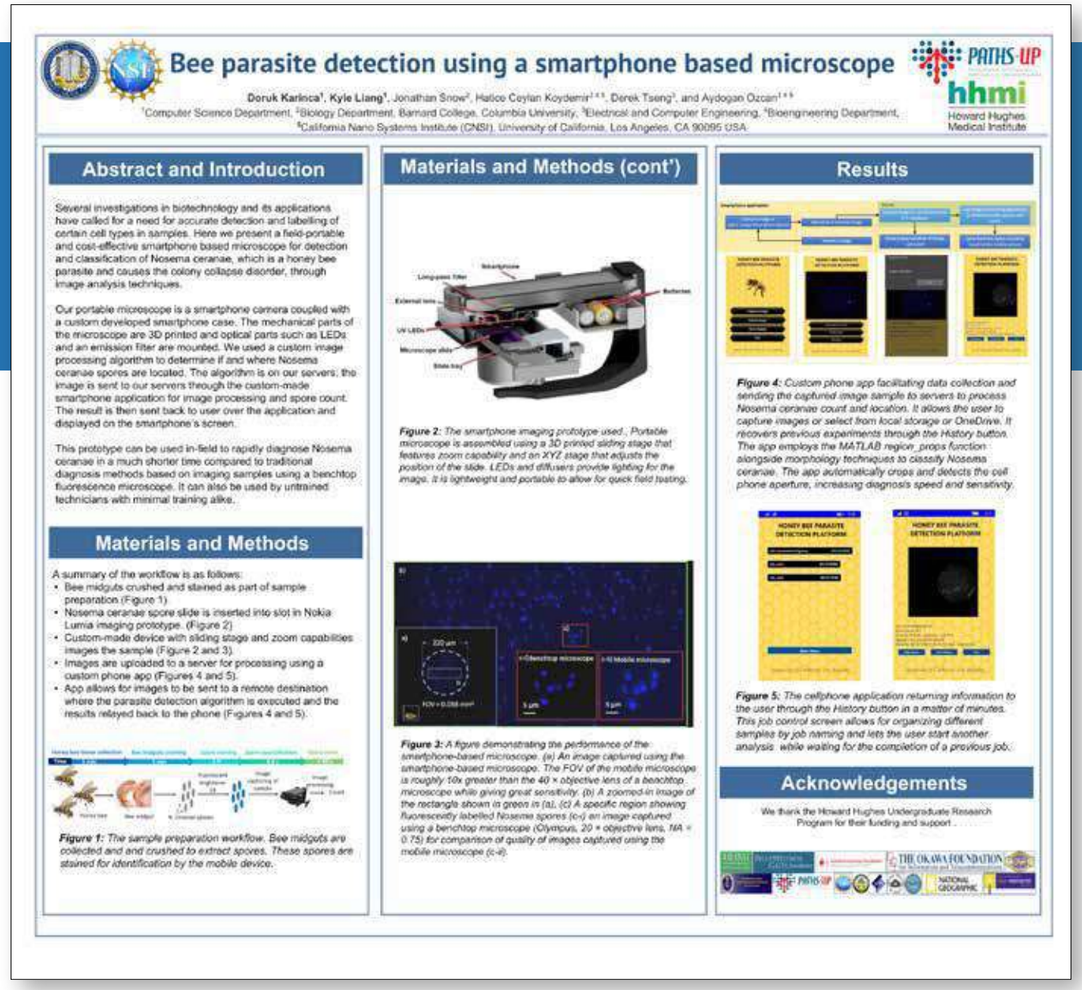

Bee parasite detection using a smartphone based microscope

Doruk Karinca[1], Kyle Liang[1], Jonathan Snow[2], Hatice Ceylan Koydemir[1,2,3], Derek Tseng[1], and Aydogan Ozcan[1,2,3]

[1]Computer Science Department, [2]Biology Department, Barnard College, Columbia University, [3]Electrical and Computer Engineering, [4]Bioengineering Department, [5]California Nano Systems Institute (CNSI), University of California, Los Angeles, CA 90095 USA

PATHS UP

hhmi Howard Hughes Medical Institute

Abstract and Introduction

Several investigations in biotechnology and its applications have called for a need for accurate detection and labelling of certain cell types in samples. Here we present a field-portable and cost-effective smartphone based microscope for detection and classification of Nosema ceranae, which is a honey bee parasite and causes the colony collapse disorder, through image analysis techniques.

Our portable microscope is a smartphone camera coupled with a custom developed smartphone case. The mechanical parts of the microscope are 3D printed and optical parts such as LEDs and an emission filter are mounted. We used a custom image processing algorithm to determine if and where Nosema ceranae spores are located. The algorithm is on our servers; the image is sent to our servers through the custom-made smartphone application for image processing and spore count. The result is then sent back to user over the application and displayed on the smartphone's screen.

This prototype can be used in-field to rapidly diagnose Nosema ceranae in a much shorter time compared to traditional diagnosis methods based on imaging samples using a benchtop fluorescence microscope. It can also be used by untrained technicians with minimal training alike.

Materials and Methods

A summary of the workflow is as follows:

- Bee midguts crushed and stained as part of sample preparation (Figure 1)
- Nosema ceranae spore slide is inserted into slot in Nokia Lumia imaging prototype. (Figure 2)
- Custom-made device with sliding stage and zoom capabilities images the sample (Figure 2 and 3).
- Images are uploaded to a server for processing using a custom phone app (Figures 4 and 5).
- App allows for images to be sent to a remote destination where the parasite detection algorithm is executed and the results relayed back to the phone (Figures 4 and 5).

Figure 1: The sample preparation workflow. Bee midguts are collected and and crushed to extract spores. These spores are stained for identification by the mobile device.

Materials and Methods (cont')

Figure 2: The smartphone imaging prototype used., Portable microscope is assembled using a 3D printed sliding stage that features zoom capability and an XYZ stage that adjusts the position of the slide. LEDs and diffusers provide lighting for the image. It is lightweight and portable to allow for quick field testing.

Figure 3: A figure demonstrating the performance of the smartphone-based microscope. (a) An image captured using the smartphone-based microscope. The FOV of the mobile microscope is roughly 10x greater than the 40 × objective lens of a benchtop microscope while giving great sensitivity. (b) A zoomed-in image of the rectangle shown in green in (a). (c) A specific region showing fluorescently labelled Nosema spores (c-i) an image captured using a benchtop microscope (Olympus, 20 × objective lens, NA = 0.75) for comparison of quality of images captured using the mobile microscope (c-ii).

Results

Figure 4: Custom phone app facilitating data collection and sending the captured image sample to servers to process Nosema ceranae count and location. It allows the user to capture images or select from local storage or OneDrive. It recovers previous experiments through the History button. The app employs the MATLAB region_props function alongside morphology techniques to classify Nosema ceranae. The app automatically crops and detects the cell phone aperture, increasing diagnosis speed and sensitivity.

Figure 5: The cellphone application returning information to the user through the History button in a matter of minutes. This job control screen allows for organizing different samples by job naming and lets the user start another analysis while waiting for the completion of a previous job.

Acknowledgements

We thank the Howard Hughes Undergraduate Research Program for their funding and support .

Carolyn Kim

Bioengineering

Senior

LAB NAME

Seidlits Research Group

FACULTY ADVISOR

Stephanie Seidlits

DAILY LAB SUPERVISOR

Jesse Liang

DEPARTMENT

Bioengineering

3D Hyaluronic Acid Based Hydrogel Constructs for Directed Differentiation of Human Pluripotent Stem Cells

In development, several cues work in tandem to direct specification of the three germ layers, which ultimately form the organism. Identifying these cues is of great interest in tissue engineering with the hopes of identifying critical processes required for organ formation. Soluble cues are established in literature as essential signaling components. Insoluble cues also govern cellular processes, but are less explored. To investigate the individual and synergistic effects of these dynamic cues on human embryonic stem cell (hESC) differentiation, a highly tunable biomaterials system in the form of a 3D hyaluronic acid (HA) based hydrogel was developed. Hydrogels were prepared via photo initiated radical crosslinking of thiolated HA with norbornene terminated polyethylene glycol (PEG) and thiol terminated PEG. hESCs were encapsulated as uniform embryoid bodies. Acquisition of germ layer phenotypes was interrogated by immunostaining for markers of pluripotency (OCT4) and the three germ layers. Cell proliferation, survival, and morphology were also interrogated. The effect of gel moduli on hESCs was explored by providing either a soft or stiff hydrogel. In both conditions, hESCs survived and differentiated. 1 and 2 week cultures demonstrated that hESCs maintained OCT4 expression and exhibited differing amounts of commitment to the three germ layers. Immunostaining for HOXB4 will provide insight into whether different gel compressive moduli can affect the interpretation of soluble cues and ultimately bias cell fate decisions.

3D Hyaluronic Acid – Based Hydrogel Constructs For Directed Differentiation of Human Pluripotent Stem Cells

[1]**Carolyn Kim**, [1]Jesse Liang, [1]Alireza Sohrabi, [1]Stephanie Seidlits

[1] Department of Bioengineering, Henry Samueli School of Engineering, University of California Los Angeles

BACKGROUND

- Tissue engineering has the possibilities of recreating whole tissues and organs from single cells.
- The soluble and insoluble cues in the extracellular matrix (ECM) impact cellular activity by providing structure, providing growth factors, and transducing mechanical signals.
- The complexity of cell interactions with their local environment makes it difficult to distinguish independent and synergistic effects of these parameters on cell behavior
- Synthetic hydrogels can be used to model the cellular microenvironment and understand cellular response to external cues
- Gel stiffness and diffusivity are important to investigate because they can affect cell signaling and nutrient transport
- In this initial work we present a method for precise control and characterization of these properties

GEL FABRICATION SCHEME

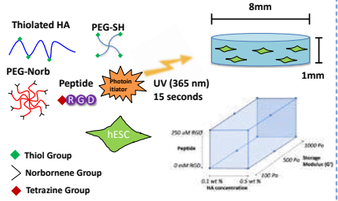

- Gel networks are formed by a thiol-ene (molar ratio 1.0:1.2) chemistry with LAP as the radical generator
- Protein inspired peptides are conjugated onto PEG-norb via Diels-Alder reaction
- Gel solution is exposed to 365 nm light (3-6 mW/cm^2) for 15 seconds

GEL CHARACTERIZATION

Mechanics

To characterize the viscoelastic properties of the hydrogels, we report the storage moduli (G'). Gells swell in PBS overnight, and then a TA Instruments rheometer is used with a 8mm parallel plate to obtain data.

Diffusion

FITC-Dextran infuses at 1mg/ml for 24 hours into gels at 37C. Gels are transferred to PBS and fractional mass release is determined with fluorescence readings of samples collected at varying timepoints.

RESULTS

Hydrogel Stiffness

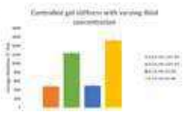

- Able to achieve two different stiffnesses: soft gels around 500 Pa and stiff gels around 1200 Pa
- Stiffness achieved regardless of HA concentration

Diffusivity of FITC-Dextran

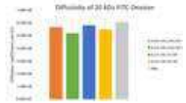

- Diffusion was the same for both stiffnesses and HA concentrations as PBS
- Stiffness did not compromise diffusion of 20 kDa proteins

Cell Viability

UV

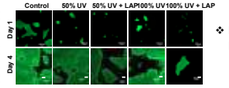

- Minimal damage to proliferation

Single Cells vs. Embryoid Bodies

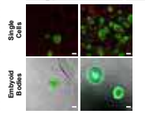

- Single cells: irregular shapes, nonuniform sizes, many dead cells
- Embryoid Bodies (EB): very round, uniform, minimal cell death

Reproducible Embryoid Bodies

- Consistent and reproducible EBs
- 250 cells/μwell chosen for experiments because most practical

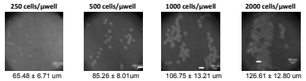

Interregation

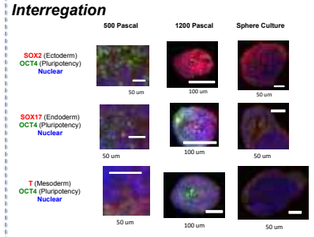

- SOX2 nuclear in all conditions
- SOX17 only nuclaer in stiff and sphere cultures
- T nonnuclear staining

CONCLUSIONS

- The work demonstrates a method for fabrication of hydrogels where storage modulus, HA concentration, and peptide presentation can be tuned in an orthogonal manner
- Diffusion and rheological studies confirm functional equivalency of gels
- Efficient and reproducible embryoid body production via Aggrewell confirms consistent encapsulation conditions
- Preliminary data suggests SOX17 (Endoderm Marker) is only present in stiff and sphere cultures

FUTURE DIRECTIONS

- Following up protein interrogation with RT-PCR
- Investigate downstream transducers of mechanics (YAP/TAZ)
- Quantifying contribution of gel parameters towards specific cell phenotypes using linear mixed models
- Increasing throughput of this gel platform to allow for efficient screening of design space
- Exploring new pluripotent cell lines as well as other cell types (glioma stem cells)
- Guiding stem cell differentiation according to protocols in literature

ACKNOWLEDGEMENTS

Funding sources: NIH Training Grant in Genomic Analysis and Interpretation T32HG002536

Acknowledgements to the Microscopic Techniques Laboratory of the UCLA Brain Research Institute and the UCLA HSSEAS Undergraduate Research Program.

Chance Kuo

Bioengineering

Junior

LAB NAME

Schmidt Lab at UCLA - Biohybrid Microsystems Laboratory

FACULTY ADVISOR

Jacob Schmidt

DAILY LAB SUPERVISOR

Shiv Acharya

DEPARTMENT

Bioengineering

A Matlab Algorithm for the Analysis of Protein-Nanopore Data Collected Using Hydrogels

Artificial nanopores are powerful tools for single-molecule analysis, and in particular are promising for protein identification and characterization. Our lab is working on a method involving hydrogels that provides more high-accuracy information from protein-nanopore measurements than previous techniques. However, the characteristics of data resulting from hydrogel use make analysis with existing computer algorithms difficult. We hypothesized that this issue could be solved with an algorithm based on image analysis, specifically the method of Canny edge detection. Thus, we designed a Matlab script that uses a modified version of this method and tested it alongside two programs commonly used for nanopore data analysis (ClampFit and Transalyzer). Mock data traces with known parameters were analyzed using the three programs, allowing performance comparisons on data with the characteristics of hydrogel use. Experimental nanopore data collected using hydrogels was then analyzed for further comparison of output statistics. The results show that our script is more reliable than the other programs for the tested data. It is able to analyze high-noise data with greater accuracy than ClampFit and can analyze data with high event frequencies and long translocation times where Transalyzer fails. These assessments indicate that Canny edge detection provides a working method and that our program offers a reliable algorithm for analyzing protein-nanopore data obtained using hydrogels.

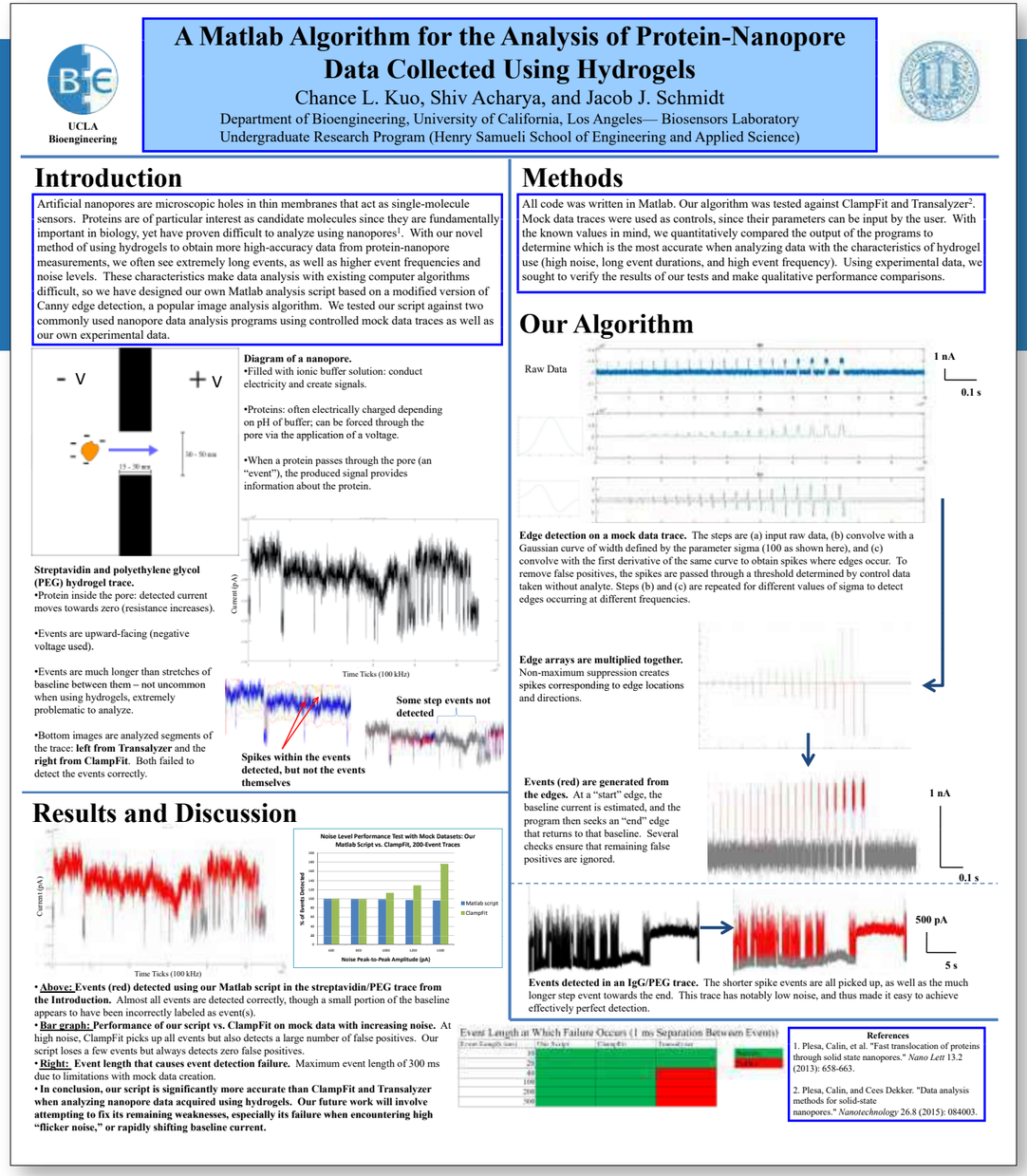

A Matlab Algorithm for the Analysis of Protein-Nanopore Data Collected Using Hydrogels

Chance L. Kuo, Shiv Acharya, and Jacob J. Schmidt

Department of Bioengineering, University of California, Los Angeles— Biosensors Laboratory

Undergraduate Research Program (Henry Samueli School of Engineering and Applied Science)

UCLA Bioengineering

Introduction

Artificial nanopores are microscopic holes in thin membranes that act as single-molecule sensors. Proteins are of particular interest as candidate molecules since they are fundamentally important in biology, yet have proven difficult to analyze using nanopores[1]. With our novel method of using hydrogels to obtain more high-accuracy data from protein-nanopore measurements, we often see extremely long events, as well as higher event frequencies and noise levels. These characteristics make data analysis with existing computer algorithms difficult, so we have designed our own Matlab analysis script based on a modified version of Canny edge detection, a popular image analysis algorithm. We tested our script against two commonly used nanopore data analysis programs using controlled mock data traces as well as our own experimental data.

Diagram of a nanopore.
•Filled with ionic buffer solution: conduct electricity and create signals.

•Proteins: often electrically charged depending on pH of buffer; can be forced through the pore via the application of a voltage.

•When a protein passes through the pore (an "event"), the produced signal provides information about the protein.

Streptavidin and polyethylene glycol (PEG) hydrogel trace.
•Protein inside the pore: detected current moves towards zero (resistance increases).

•Events are upward-facing (negative voltage used).

•Events are much longer than stretches of baseline between them – not uncommon when using hydrogels, extremely problematic to analyze.

•Bottom images are analyzed segments of the trace: **left from Transalyzer** and the **right from ClampFit**. Both failed to detect the events correctly.

Methods

All code was written in Matlab. Our algorithm was tested against ClampFit and Transalyzer[2]. Mock data traces were used as controls, since their parameters can be input by the user. With the known values in mind, we quantitatively compared the output of the programs to determine which is the most accurate when analyzing data with the characteristics of hydrogel use (high noise, long event durations, and high event frequency). Using experimental data, we sought to verify the results of our tests and make qualitative performance comparisons.

Our Algorithm

Edge detection on a mock data trace. The steps are (a) input raw data, (b) convolve with a Gaussian curve of width defined by the parameter sigma (100 as shown here), and (c) convolve with the first derivative of the same curve to obtain spikes where edges occur. To remove false positives, the spikes are passed through a threshold determined by control data taken without analyte. Steps (b) and (c) are repeated for different values of sigma to detect edges occurring at different frequencies.

Edge arrays are multiplied together. Non-maximum suppression creates spikes corresponding to edge locations and directions.

Events (red) are generated from the edges. At a "start" edge, the baseline current is estimated, and the program then seeks an "end" edge that returns to that baseline. Several checks ensure that remaining false positives are ignored.

Events detected in an IgG/PEG trace. The shorter spike events are all picked up, as well as the much longer step event towards the end. This trace has notably low noise, and thus made it easy to achieve effectively perfect detection.

Results and Discussion

• **Above:** **Events (red) detected using our Matlab script in the streptavidin/PEG trace from the Introduction.** Almost all events are detected correctly, though a small portion of the baseline appears to have been incorrectly labeled as event(s).
• **Bar graph:** **Performance of our script vs. ClampFit on mock data with increasing noise.** At high noise, ClampFit picks up all events but also detects a large number of false positives. Our script loses a few events but always detects zero false positives.
• **Right:** **Event length that causes event detection failure.** Maximum event length of 300 ms due to limitations with mock data creation.
• **In conclusion, our script is significantly more accurate than ClampFit and Transalyzer when analyzing nanopore data acquired using hydrogels. Our future work will involve attempting to fix its remaining weaknesses, especially its failure when encountering high "flicker noise," or rapidly shifting baseline current.**

References

1. Plesa, Calin, et al. "Fast translocation of proteins through solid state nanopores." *Nano Lett* 13.2 (2013): 658-663.

2. Plesa, Calin, and Cees Dekker. "Data analysis methods for solid-state nanopores." *Nanotechnology* 26.8 (2015): 084003.

Jasmine Kwong

Bioengineering

Sophomore

LAB NAME

Nelson Lab

FACULTY ADVISOR

Stanley Nelson

STUDENT DAILY LAB SUPERVISOR

Hane Lee

DEPARTMENT

Human Genetics

De Novo Variant in KMT2A and DYNC1H1 Respectively Results in Wiedemann-Steiner Syndrome and Charcot-Marie-Tooth Disease

For patients that exhibit a constellation of symptoms that do not align with clear-cut phenotypes of diseases, receiving the molecular diagnosis through traditional forms of testing, such as microarray analysis, single gene, or gene panel testing, can be challenging. However, through Clinical Exome Sequencing (CES) that surveys all genes simultaneously, higher molecular diagnostic yields can be achieved in a less timeconsuming and more cost-effective manner. Two undiagnosed cases were subject to CES as part of the Undiagnosed Diseases Network (UDN). Following the standard protocol from blood collection to variant calling, a variant list for each family was annotated and filtered by population minor allele frequency, inheritance mode, phenotype, and variant pathogenicity. Case 1 was a 4-year-old female with developmental delay, hypotonia, and dysmorphic features and was found with a de novo variant in KMT2A associated with autosomal dominant (AD) Wiedemann-Steiner Syndrome. Case 2 was a 15-year-old male with muscular atrophy, waddling gait, and cognitive delay, and a paternally inherited heterozygous variant in DYNC1H1 was identified for AD Charcot- Marie-Tooth Disease; the patient's father also turned out to be mildly affected with mosaicism. Besides providing greater insight to the genetic cause of the disorder and resulting in better clinical management, employing CES resulted in a faster diagnosis – allowing for greater emphasis and efforts to be placed towards treating patients with rare Mendelian disorders.

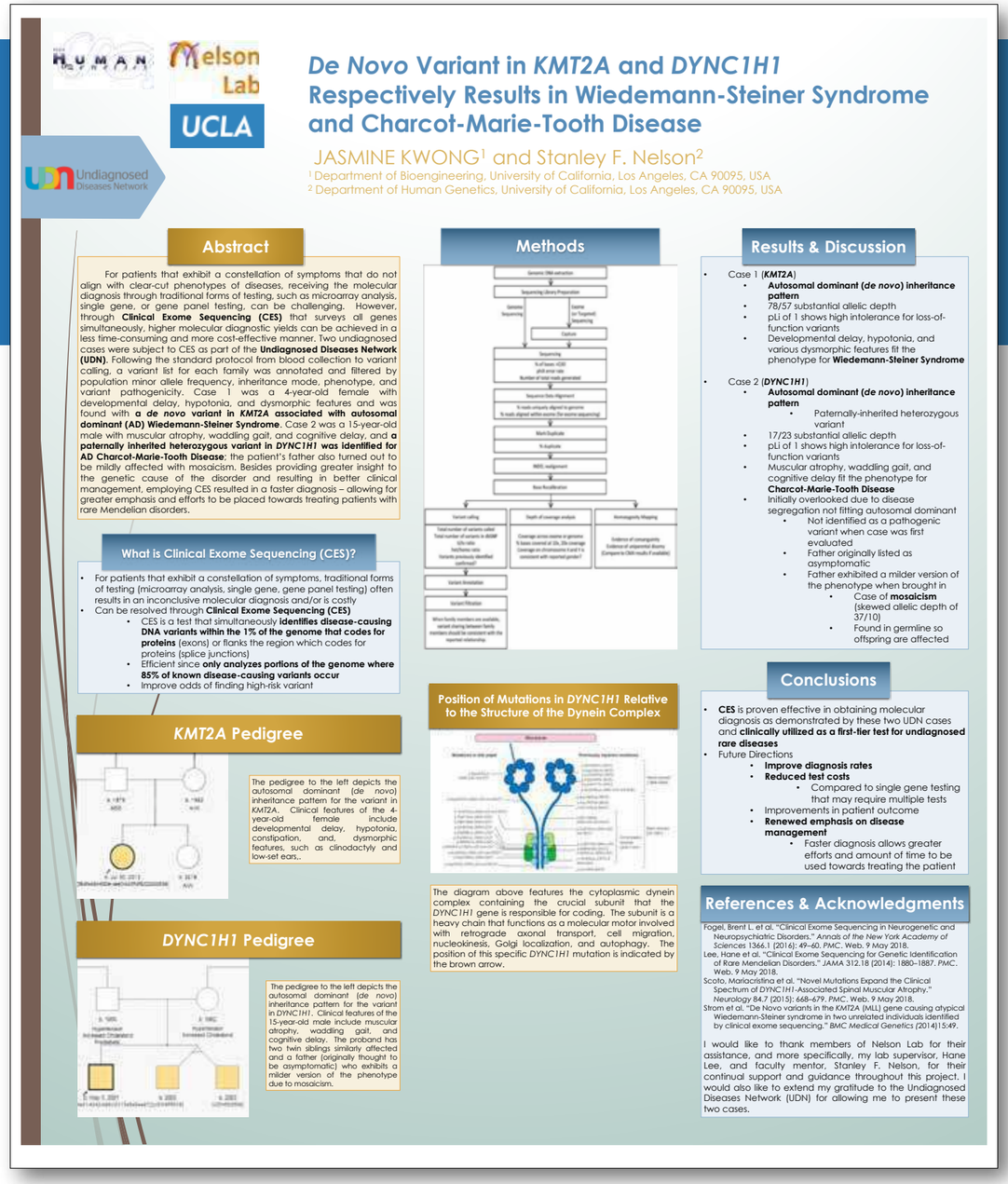

Jeffrey Lam

Bioengineering

Senior

LAB NAME

Di Carlo Laboratory

FACULTY ADVISOR

Dino Di Carlo

DAILY LAB SUPERVISOR

Manjima Dhar

DEPARTMENT

Bioengineering

Adapting the Vortex Isolation Method to Clinical and Research Applications

Circulating tumor cells (CTCs) are rare cells in the blood of cancer patients, and have been implicated as a mechanism for cancer metastasis. These cells could be used as a companion to current diagnostics or prognostics. Further research on the phenotypes of these cells could elucidate new therapies and the pathways by which cancer spreads. CTCs can be isolated from blood using several technologies that either rely on cell size or surface markers. We use the Vortex device, a microfluidic device that traps cells based on size. After upstream cell isolation, cells are transferred into micro droplets for phenotypic and genotypic analysis. This procedure involves several device manipulations. In order to make this device easy to use in research and clinical settings, improvements must be made to streamline efficiency and make it more versatile. We automated the process by creating device mounts and a LABVIEW program that eliminates error due to human intervention. Secondly, we demonstrate the versatility of the Vortex method by using it to measure matrix metalloproteinase (MMP) activity in CTCs, as this is a suspected mechanism of cancer metastasis. We also adapt the Vortex method to identify for common genetic mutations in cancer cells by capturing circulating tumor DNA using silica beads and analyzing them using droplet based digital PCR.

UCLA ENGINEERING

ADAPTING THE VORTEX ISOLATION METHOD TO CLINICAL AND RESEARCH APPLICATIONS

Jeffrey Lam[1], Manjima Dhar[1], and Dino Di Carlo[1]

1 Department of Bioengineering, University of California, Los Angeles, Los Angeles, CA, USA

1. Vortex Method Overview

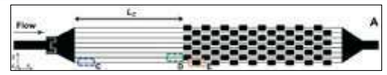

- Circulating Tumor Cells (CTCs) are rare cells implicated in cancer metastasis
- Isolation of these cells based on their larger size (compared to other components of blood) is possible with Vortex[1]

Vortex Isolation Method

1. Isolate CTCs from patient blood using Vortex chip
2. Introduce substrate into Vortex chip, break vortices and release CTCs by altering the flow
3. Use step emulsification droplet generator to move CTCs into droplets with substrate
4. Image droplets, observe intensity of fluorescence (dependent on amount of substrate cleaved)

Necessary Improvements

- Automation to lower error due to human intervention
- Stands to immobilize setup and allow for consistent experiments
- Expansion of method to other applications to improve efficacy of research

2. 3-D Printing Stands using AutoCAD

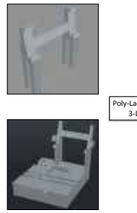

Poly-Lactic Acid (PLA) 3-D Printing

- Vortex stand allowed to shift along base of droplet generator stand
- Devices put as close as possible to reduce resistance from wire length

3. Automating the Vortex Method using LabVIEW

2 pump daisy-chained system

Criteria

- 3 Syringe pumps: Substrate, Cells, Wash
- Continual Flow Changes
- Pinch Valve Swap
- Minimal delay between steps
- Pullback of "Cells" syringe pump during final stage to relieve backflow pressure

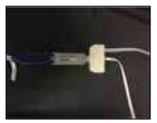

USB -> RS-232 -> RJ11

Results

- 200 ms delay in 2 pump system, staggered commands necessary for correct timings
- Signal attenuation present when using RJ-11 splitter, daisy chaining necessary but will lead to greater delays in 2nd and 3rd pumps
- Pullback done by adding reverse command to "Cells" syringe and increasing pump speed in "Substrate" in final step

4. Analysis of ctDNA using Vortex

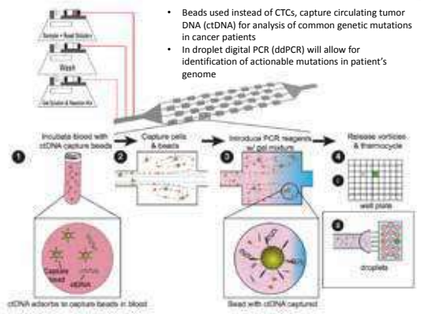

- Beads used instead of CTCs, capture circulating tumor DNA (ctDNA) for analysis of common genetic mutations in cancer patients
- In droplet digital PCR (ddPCR) will allow for identification of actionable mutations in patient's genome

Implementation Tests

- ctDNA–Silica bead affinity with and without Vortex
- Silica bead isolation using Vortex method: 1 bead per droplet (**FOCUS**)
- ctDNA amplification in droplet

5. Using Silica beads in conjunction with Vortex

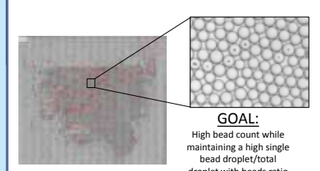

GOAL:

High bead count while maintaining a high single bead droplet/total droplet with beads ratio

Analysis Method

- 2 droplet generator sizes and 4 different bead counts used
- Droplet Generators imaged under brightfield
- Droplets individually screened and marked for either 1 bead/droplet (red) or multiple beads/droplet (teal)

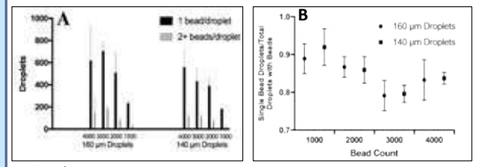

Results

- High Variability in 3000 and 4000 bead tests, likely due to bead-bead interactions in vortices as well as at the boundary between vortex chamber and channel
- Capture Efficiency below 50% for all inputs
- 2000 and 1000 bead tests had best single bead droplet to total droplets with beads ratio, similar ratio of beads captured to beads inputted
- Better Vortex maintenance and Pluronics necessary for smoother bead flow
- New tests necessary following introduction of Gelatin droplets and ctDNA blood samples

6. References

[1] Sollier E. et al. (2014) "Size-Selective collection of circulating tumor cells using Vortex technology." Lab on a Chip.

Hannah Lin

Computer Science

Sophomore

LAB NAME
The Tarling-Vallim Lab

FACULTY ADVISOR
Thomas Vallim

DAILY LAB SUPERVISOR
Jenny Link

DEPARTMENT
Biological Chemistry

RNA-Binding Proteins ZFP36 and ZFP36L1 Post-Transcriptionally Regulate Mouse Liver Gene Expression in LPS-Induced Inflammation

Recent findings in our lab demonstrate that ZFP36 and ZFP36L1 are RNA binding proteins that post-transcriptionally modulate mRNA expression. Additionally, preliminary data show increased Zfp36 and Zfp36l1 levels upon lipopolysaccharide (LPS) treatment. Under LPS treatment, ZFP36 and ZFP36L1 may potentially influence many other mRNA transcripts. To examine the role of ZFP36 and ZFP36L1 in regulating liver gene expression, we treated Zfp36, Zfp36l1 double knockout mice (DKO) with LPS and collected liver tissue. We compared liver RNA-seq data from 4 groups of mice: wild-type (WT) mice treated with vehicle, WT mice treated with LPS, DKO mice treated with vehicle, and DKO mice treated with LPS. In both WT and DKO groups, over 10,000 genes were differentially expressed between LPS- and vehicle-treated mice. We found that ZFP36 and ZFP36L1 specifically upregulated 858 genes and downregulated 864 genes in LPS-treated mice compared to vehicle. The upregulated genes are enriched for RNA transport and ubiquitin-mediated proteolysis. In the RNA transport pathway, the genes include eukaryotic translation initiation factor subunits, which, like ZFP36 and ZFP36L1, are also post-transcriptional regulators. The downregulated genes are enriched for metabolic pathways. These genes include NADH dehydrogenase subcomplexes that may need to be suppressed during inflammation. As a whole, our findings suggest that ZFP36 and ZFP36L1 play important roles in mediating LPS-induced inflammation in the liver by post-transcriptionally regulating mRNA.

RNA-Binding Proteins ZFP36 and ZFP36L1 Post-Transcriptionally Regulate Mouse Liver Gene Expression in LPS-Induced Inflammation

Hannah Lin[1], Angela Cheng[2], Abigail Aleman[2], Jenny C. Link[3], Elizabeth J. Tarling[3], and Thomas Q. de Aguiar Vallim[2,3]

[1]Department of Computer Science, [2]Department of Biological Chemistry, and [3]Department of Medicine, Cardiology, University of California, Los Angeles

UCLA The Tarling-Vallim Lab

Introduction

In this study, we examined what pathways in the inflammatory response are mediated by ZFP36 and ZFP36L1.

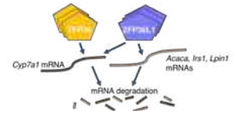

- ZFP36 and ZFP36L1 are RNA binding proteins that post-transcriptionally modulate mRNA expression (Tarling et al, 2017).

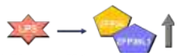

- *Zfp36* and *Zfp36l1* levels increase upon lipopolysaccharide (LPS) treatment.

We wondered what mRNA transcripts are influenced by ZFP36 and ZFP36L1 under LPS treatment.

Design

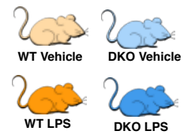

We had 4 groups of mice: (1) wild-type (WT) mice treated with vehicle, (2) WT mice treated with LPS, (3) *Zfp36* and *Zfp36l1* DKO mice treated with vehicle, and (4) DKO mice treated with LPS.

Methods

1. We collected liver tissue and extracted RNA from the 4 groups of mice.
2. RNA-seq was performed with Illumina HiSeq 4000.
3. Reads were demultiplexed and trimmed with htSeqTools and cutadapt. The quality of the reads was checked with FastQC.
4. Reads were mapped with HISAT2 and merged with Picard Tools before features were counted with HTSeq. Counts were analyzed with DESeq2 in R.

Results

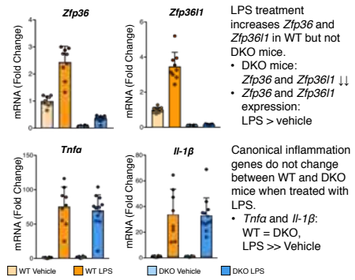

LPS treatment increases *Zfp36* and *Zfp36l1* in WT but not DKO mice.
- DKO mice: *Zfp36* and *Zfp36l1* ↓↓
- *Zfp36* and *Zfp36l1* expression: LPS > vehicle

Canonical inflammation genes do not change between WT and DKO mice when treated with LPS.
- *Tnfα* and *Il-1β*: WT = DKO, LPS >> Vehicle

Western blots verified that ZFP36 and ZFP36L1 were not present in DKO mice.
- ZFP36 and ZFP36L1 protein levels: LPS > vehicle

Deficiency of *Zfp36* and *Zfp36l1* altered gene expression in liver.

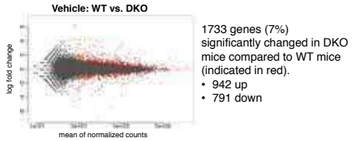

1733 genes (7%) significantly changed in DKO mice compared to WT mice (indicated in red).
- 942 up
- 791 down

LPS treatment altered over a third of expressed liver genes.

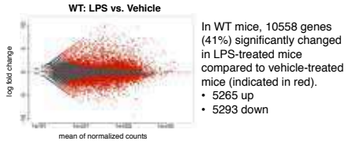

In WT mice, 10558 genes (41%) significantly changed in LPS-treated mice compared to vehicle-treated mice (indicated in red).
- 5265 up
- 5293 down

ZFP36 and ZFP36L1 specifically alter the expression of hundreds genes under LPS-induced inflammation.

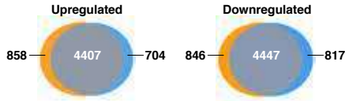

Results (cont.)

Upregulated genes are enriched for RNA transport and ubiquitin-mediated proteolysis. Downregulated genes are enriched for metabolic pathways.

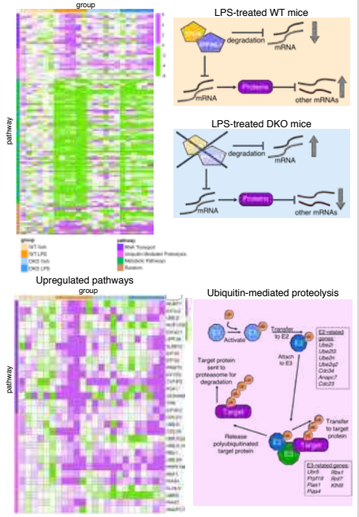

Conclusion

Our data suggest that ZFP36 and ZFP36L1 have broad impacts in modulating gene expression downstream of LPS signaling.

Acknowledgements

- Tarling et al. *J Clin Invest.* 2017

- HSSEAS Undergraduate Research Program

Zubin Mishra

Chemical Engineering

Junior

LAB NAME

Simonetti Research Group

FACULTY ADVISOR

Dante Simonetti

DAILY LAB SUPERVISOR

Faisal Alshafei

DEPARTMENT

Chemical and Biomolecular Engineering

The Effects of Metal Dopants on the Stability of Calcium Oxide Nanofibers in the Adsorption of CO2

Hydrogen is a basic building block of energy and is touted by many as a clean, flexible energy carrier that has the potential to cause a paradigm shift in the energy market. Sorption-enhanced steam methane reforming (SE-SMR) is an emerging technology for directly producing high concentrations of hydrogen. However, the adoption of this technique is hindered by the current state of high temperature adsorbents for CO2 capture. These sorbents suffer from the rapid decay of their initial CO2 uptake capacity with repeated cycles of carbonation and calcination due to sintering, pore plugging, and particle agglomeration. To alleviate the dramatic decay in CO2 uptake capacity, inexpensive metal doped CaO-based sorbents were synthesized via electrospinning. Metals from Groups 2, 3, 4, 12 and 13 on the periodic table of elements were incorporated in the highly porous CaO fibrous structure, to develop sorbents that will attenuate the effects associated with the repeated cycling of these materials and increase their CO2 uptake capacities.

The results indicate a promising opportunity for the application of electrospun materials

in SE-SMR. The reactivity of the doped CaO nanofibers were tested using CO2 thermogravimetry. The nanofibers were characterized using X-ray diffraction (XRD), energy-dispersive X-ray spectroscopy (EDS), and scanning electron microscopy (SEM) to elucidate information about crystallite size and crystalline phase, chemical composition, and nanofiber morphology, respectively.

The Effects of Metal Dopants on the Stability of Calcium Oxide Nanofibers in the Adsorption of CO_2

Zubin Mishra, Faisal Alshafei, Luke Minardi, and Dante Simonetti

Department of Chemical and Biomolecular Engineering, University of California – Los Angeles

Motivation

Hydrogen is a basic building block of energy, widely used in petroleum, chemical, energy, and metallurgical industries and touted by many as a clean, flexible energy carrier with the potential to cause a paradigm shift in the energy market. Sorption-enhanced steam methane reforming (SE-SMR) is an emerging technology for directly producing high concentrations of hydrogen. However, the adoption of this technique is hindered by the current state of high temperature adsorbents for CO_2 capture. These sorbents suffer from the rapid decay of their initial CO_2 uptake capacity with repeated cycles of carbonation and calcination due to sintering, pore plugging, and particle agglomeration.

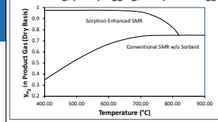

Figure 1. Comparison of hydrogen molar fraction produced through steam methane reforming with and without the use of a sorbent [1].

Introduction

The focus of this research was to synthesize inexpensive metal doped CaO-based sorbents via electrospinning and compare their performance to alternatively synthesized sorbents in a multi-cycle process of carbonation and decarbonation. Metal A, Metal B, Metal C, Metal D, and Metal E were then incorporated in the highly porous CaO fibrous structure to develop sorbents that will attenuate the effects associated with the repeated cycling of these materials and increase their CO_2 uptake capacities. The capacity and stability of these metal doped sorbents were compared to nanofibers of pure CaO.

Electrospinning of CaO Nanofibers

1. Solution Preparation:

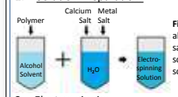

Figure 2-1. Polymer was dissolved in an alcohol solvent while calcium and metal salts were dissolved in water. The two solutions were combined to create the solution for electrospinning.

2. Electrospinning:

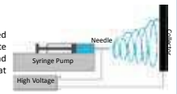

Figure 2-2. Electrospinning was conducted at a high voltage, with a set extrusion rate and separation between the collector and needle. Nanofibers were collected at room temperature on aluminum foil.

3. Thermal Treatment:

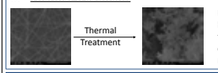

Figure 2-3. Nanofibers were heat-treated for several hours to decompose the polymer chains and produce Metal/Ca nanofibers.

Hydrothermal Synthesis of CaO Nanoparticles

1. Solution Preparation:

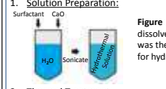

Figure 3-1. Calcium oxide and surfactant were dissolved in water, and the resulting solution was then sonicated for several hours to prepare for hydrothermal treatment.

2. Thermal Treatment:

Figure 3-2. The collected solid was washed and then dried overnight. Afterwards, it was heat-treated at to convert calcium hydroxide to calcium oxide.

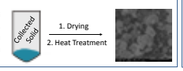

Thermal Treatment of Ca-Acetate and Marble

1. Particle Preparation:

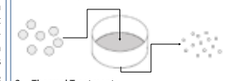

Figure 4-1. Calcium acetate and marble was crushed and sieved.

2. Thermal Treatment:

Figure 4-2. The collected particles were heat-treated to produce calcium oxide.

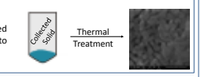

Comparison of Synthesis Techniques

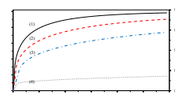

Figure 5. Sorption capacities and conversions of (1) CaO-nanofibers, (2) CaO-acetate, (3) CaO-nitrate, and (4) CaO-marble.

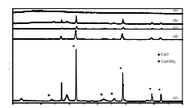

Figure 6. X-Ray diffraction of the synthesized (a) Polymer-Ca nanofibers, (b) CaO-nanofibers after thermal treatment, (c) CaO-acetate, (d) CaO-nitrate, and (e) CaO-marble. XRD peaks confirm the presence of pure CaO.

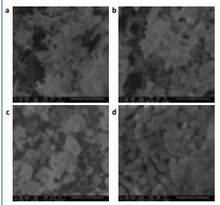

Figure 7. SEM images of (a) CaO-nanofibers after thermal treatment, (b) CaO-acetate, (c) CaO-nitrate, and (d) CaO-marble. Upon heat-treatment, the polymer chains are decomposed and the smooth, continuous, and cylindrical nanofibers are transformed to segmented fibers comprised of calcium oxide nanoparticles.

Table 1. Comparison of surface area, pore volume, pore diameter, and crystallite size for each synthesis technique.

Sorbent	S_{BET}	V_{pore}	Pore Diameter	Crystallite Size
CaO-marble	7.6	0.034	9.5	84
CaO-acetate	17	0.110	13.9	33
CaO-nitrate	16	0.010	18.6	35
CaO-nanofibers	16	0.092	13.1	39

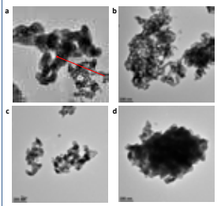

Figure 8. TEM images of (a) CaO-nanofibers after thermal treatment, (b) CaO-acetate, (c) CaO-nitrate, and (d) CaO-marble. TEM images show that despite larger crystallite sizes, the nanofibers have numerous large pores.

Metal Doped CaO Nanofibers

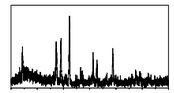

Figure 9. X-ray diffraction confirms the presence of CaO and metal oxides.

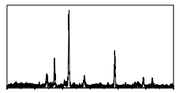

Figure 10. X-ray diffraction confirms the presence of CaO and metal oxides.

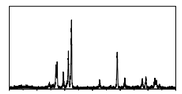

Figure 11. . X-ray diffraction confirms the presence of CaO and metal oxides.

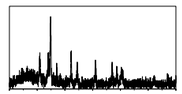

Figure 12. . X-ray diffraction confirms the presence of CaO and metal oxides.

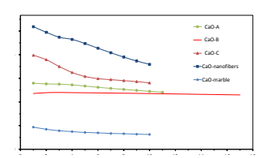

Figure 13. Sorption capacities of the metal doped CaO nanofibers over several cycles of carbonation and calcination.

Conclusions

The results indicate a promising opportunity for the application of electrospun materials in SE-SMR. Calcium oxide nanofibers doped with Metal B exhibited exceptional stability when compared to pure calcium oxide nanofibers and other dopants. These improvements in CO_2 sequestration materials have the potential to reduce costs of CO_2 capture by offering greater cost advantage than current conventional technologies (e.g. amine scrubbing) due to the high availability and low cost of CaO based sorbents.

Acknowledgements

The authors acknowledge financial support from the Henry Samueli School of Engineering and Applied Sciences and the Office of Equity, Diversity, and Inclusion at UCLA. The authors also acknowledge the Molecular & Nano Archaeology (MNA) Laboratory at UCLA Materials Science Department for use of the SEM, the J.D. McCullough Laboratory of X-ray Crystallography at UCLA Chemistry Department for use of the XRD, and the California NanoSystems Institute (CNSI) at UCLA for use of the TGA.

References

1. Barelli, L., et al. "Hydrogen production through sorption-enhanced steam methane reforming and membrane technology: a review." *Energy* 33.4 (2008): 554-570.

LAB NAME

Jenny Jay's Lab Group

FACULTY ADVISOR

Jennifer Jay

DAILY LAB SUPERVISOR

Victoria Whitener

DEPARTMENT

Civil and Environmental Engineering

Pauline Nguyen

Civil Engineering

Junior

Comparison of Antibiotic Resistance Proliferation in Secondary Treatment Processes: Trickling Filter versus Activated Sludge

The overuse of antibiotics, both medically and agriculturally, has resulted in their dissemination into the environment, posing risks regarding public health and the development of antibiotic resistant bacteria (ARB). In particular, wastewater treatment plants are important reservoirs that create favorable conditions to allow for the survival of bacterial resistance through vertical and horizontal gene transfer. In the traditional 3-step wastewater treatment process, the second step is not well-studied with respect to antibiotic resistance; it is known that activated sludge is a more efficient process for total bacterial removal although its removal efficiency of ARB is unknown. This study analyzes the ampicillin resistance shift of E. coli in two secondary treatment methods: trickling filter versus activated sludge. 24-hour composite samples of secondary influent, trickling filter effluent, and activated sludge effluent were taken from Orange County Sanitation District. These samples were diluted and filtered through a 0.45 m filter, placed onto mTEC agar plates with varying ampicillin doses, and incubated for 24 hours. It was found that 381 mg/L of ampicillin was needed to kill 90% of E. Coli for trickling filter effluent versus 153 mg/L for activated sludge effluent. This finding shows that using trickling filters as a secondary treatment method results in a bacterial community with a higher IC90 which alludes to a larger hypothesis that biofilms in trickling filters contribute to increased antibiotic resistance.

UCLA

Comparison of Antibiotic Resistance Proliferation in Secondary Treatment Processes: Trickling Filter versus Activated Sludge

Victoria Whitener, Megyn Rugh, Pauline Nguyen, Jennifer A. Jay

Department of Civil and Environmental Engineering

Introduction

- The over-prescription and abuse of antibiotics used by humans and animals from hospitals, households, animal farms, etc. eventually end up in the sewage en route to wastewater treatment plants (WWTPs).
- WWTPs are among the main sources of both antibiotic-resistant bacteria (ARB) and antibiotic-resistant genes (ARGs) because they receive sewage from various sources, and a high density of bacteria from different environments, making them a hotspot for bacteria to interact and exchange genes horizontally.

Figure 1. Vertical gene transfer of antibiotic resistance.

WWTPs were not designed for the removal of these specific contaminants!

Secondary Treatment in WWTP's

Activated Sludge

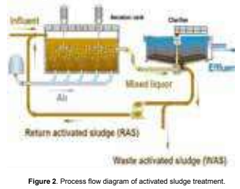

Figure 2. Process flow diagram of activated sludge treatment.

Activated sludge utilizes microbes, produced in aerobic conditions, to oxidize organic matter. The microbes are clumped together to form sludge, and can be separated from the liquid phase, forming biosolids. The sludge collected from this process is then anaerobically digested

Trickling Filter

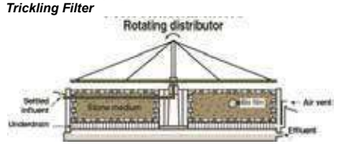

Figure 3. Process flow diagram of trickling filter treatment.

In conventional trickling filters, the effluent from primary treatment is sprinkled and evenly distributed over the rock bed, which is coated with a biological slime containing microorganisms. As the liquid trickles over the slime, oxygen and the dissolved oxygen matter from the secondary influent is diffused into the film to be metabolized by the microorganisms in the biofilm.

Biofilms

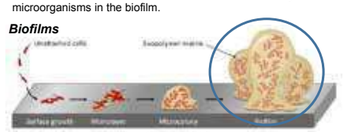

Figure 4. Formation of biofilms.

Antibiotic resistant bacteria are protected from treatment from biofilms. Biofilms can reduce the ability of antibiotics from reaching the cytoplasm of cells.

Research Objectives

Hypothesis

The resistance of *E. Coli* to ampicillin and other antibiotics increases more after secondary treatment through a trickling filter than activated sludge treatment.

Objectives

- Explore the mechanisms of secondary treatment processes as a preferential selector of antibiotic resistant bacteria
- Determine the resistance shifts in IC50 and IC90 in the secondary influent versus the trickling filter and activated sludge effluent

Methodology

1. Collect 24-hour composite samples of secondary influent, trickling filter effluent, and activated sludge effluent from Orange County Sanitation District (OCSD).
2. Using different half-log dilutions, filter each of the samples through a 0.45 µm filter using the membrane filtration technique. Plate these filtered samples onto modified mTEC agar plates, to select for enumeration of *Escherichia coli* in water, with varying ampicillin dosages (0 ppm, 2 ppm, 32 ppm, and 256 ppm). Conduct each concentration with each type of sample in triplicates.
3. Incubate plates for 2 hours at 35˚C and 22 hours at 44.5 ˚C.
4. Count the plates with 20 to 80 colonies.
5. Record and observe shifts in resistance based off of shifts in MIC 50 and MIC 90 before and after different secondary treatment methods.

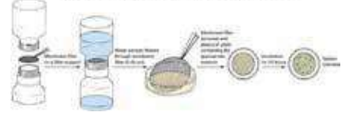

Figure 5. Process flow diagram of membrane filtration technique.

Future Directions

- Isolate *E. Coli* colonies, perform DNA extraction, and qPCR analysis of antibiotic resistant genes present in *E. Coli*
- Promote more research into antibiotic resistant bacteria (ARB) and antibiotic resistant genes (ARGs) as a regulated contaminant in wastewater treatment plants (WWTPs).

References

Bouki, C., Venieri, D., and Diamadopoulos, E. (2013). "Detection and Fate of Antibiotic Resistant Bacteria in Wastewater Treatment Plants: A Review." *Ecotoxicology and Environmental Safety*, 91, 1-9.

Dodd, M. C. (2012). Potential impacts of disinfection processes on elimination and deactivation of antibiotic resistance genes during water and wastewater treatment. Journal of Environmental Monitoring. 14(77). 1754-1771.

Huang, J., Hu, H., Lu, S., Li, Y., Tang, F., Lu, Y., and Wei, B. (2011). "Monitoring and Evaluation of Antibiotic-Resistant Bacteria at a Municipal Wastewater Treatment Plant in China." *Environment International*, 42(2012), 31-36.

Jury, K.L., Vancov, T., Stuetz, R.M., Khan, S.J. (2010). "Antibiotic resistance dissemination and sewage treatment plants." *Applied Microbiology and Microbial Biotechnology*, 509-519.

Karkman, A., Do, T. T., Walsh, F., & Virta, M. P. J. (2017). Antibiotic-Resistance Genes in Waste Water. *Trends in Microbiology*, *26*(3), 220–228. https://doi.org/10.1016/j.tim.2017.09.005

Munir, Mariya. "Occurrence and Release of Antibiotic Resistant Bacteria and Antibiotic Resistant Genes in Wastewater Utilities." Master of Science. Michigan State University, 2010. Print.

Rizzo, L., Manaia, C., Merlin, C., Schwartz, T., Dagot, C., Ploy, M.C., Michael, I., and Fatta-Kassinos, D. (2013). "Urban Wastewater Treatment Plants as Hotspots for Antibiotic Resistant Bacteria and Genes Spread Into the Environment: A Review." *Science of the Total Environment*, 447, 345-360.

Zhang, Y., Marrs, C. F., Simon, C., and Xi, C. (2009). "Wastewater Treatment Contributes to Selective Increase of Antibiotic Resistance among *Acinetobacter* spp." *Science of The Total Environment*, 407(12), 3702-3706.

Results

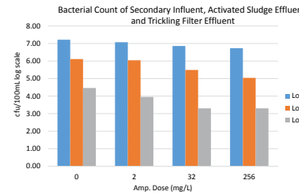

Figure 6. Bacterial counts of secondary influent, trickling filter effluent, and activated sludge effluent in log scale.

Figure 6 shows data from a preliminary experiment with 4 ampicillin doses (0, 2, 32, and 256 mg/L. The colony forming units (CFUs) are shown for secondary influent, trickling filter effluent, and secondary effluent. We see that the trickling filter is more efficient than the activated sludge at total *E. Coli* removal.

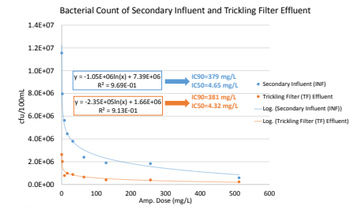

Figure 7(a). The antibiotic resistance of secondary influent versus trickling filter is compared using logarithmic curves.

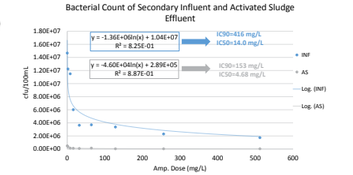

Figure 7(b). The antibiotic resistance of secondary influent versus activated sludge is compared using logarithmic curves.

Figure 7 (a and b): Colony forming units (CFUs) of *E. Coli* are plotted against the ampicillin dosages (0, 2, 8, 16, 32, 64, 128, 256, and 512 mg/L). Logarithmic trends can be seen for both the secondary influent, trickling filter effluent, and activated sludge effluent. The MIC90 is found as the ampicillin dosage at which 90% of the *E. Coli* colonies are killed. The MIC90 for the trickling filter (381 mg/L) is higher than that of the secondary influent (379 mg/L), demonstrating increased resistance.

Karina Nugroho

Biochemistry

Junior

LAB NAME

The Ozcan Research Group

FACULTY ADVISOR

Aydogan Ozcan

DAILY LAB SUPERVISOR

Hyou-Arm Joung

DEPARTMENT

Electrical Engineering

Paper-based Vertical Flow Assay for Multiplexed Analysis C-Reactive Protein (CRP) Over the Whole Serological Range

C-reactive protein (CRP) is an indication of inflammation in individuals that can be an important bio-marker for rapid and effective diagnosis of cardiovascular disease among other conditions (Black et al., 2014). In this study, we present a paper-based vertical flow assay platform for quantification of CRP over the entire serological CRP concentration range (0.1~500 µg/mL). The multiplexed assay was fabricated by dispensing antigen and antibody solutions with three different concentrations, in a multiplexed grid format, onto a sensing membrane. After the assay is performed, independent color intensity patterns are generated with antibody-conjugated gold nanoparticles corresponding to the CRP concentration. The sensing membrane containing these multiplexed spots is then imaged with a mobile-phone reader and analyzed via image processing software to quantify CRP concentration in the sample. After establishing the specific antibody-antigen pairs for our CRP sandwich immunoassay, we confirmed the independent array intensity patterns by measuring five different CRP concentrations from 0 to 50 µg/mL on a sensing membrane with 81 independent sensing spots. In the future study, we will apply a machine learning algorithm to select the optimal spotting features and improve the assay sensitivity and limit of detection over the whole serological range of CRP, resulting in a high-performance point-of-care testing (POCT) diagnostic sensor.

References

Black, S., Kushner, I., & Samols, D. (2004). C-reactive Protein. Journal of Biological Chemistry, 279(47), 48487-48490. http://dx.doi.org/10.1074/jbc.r400025200

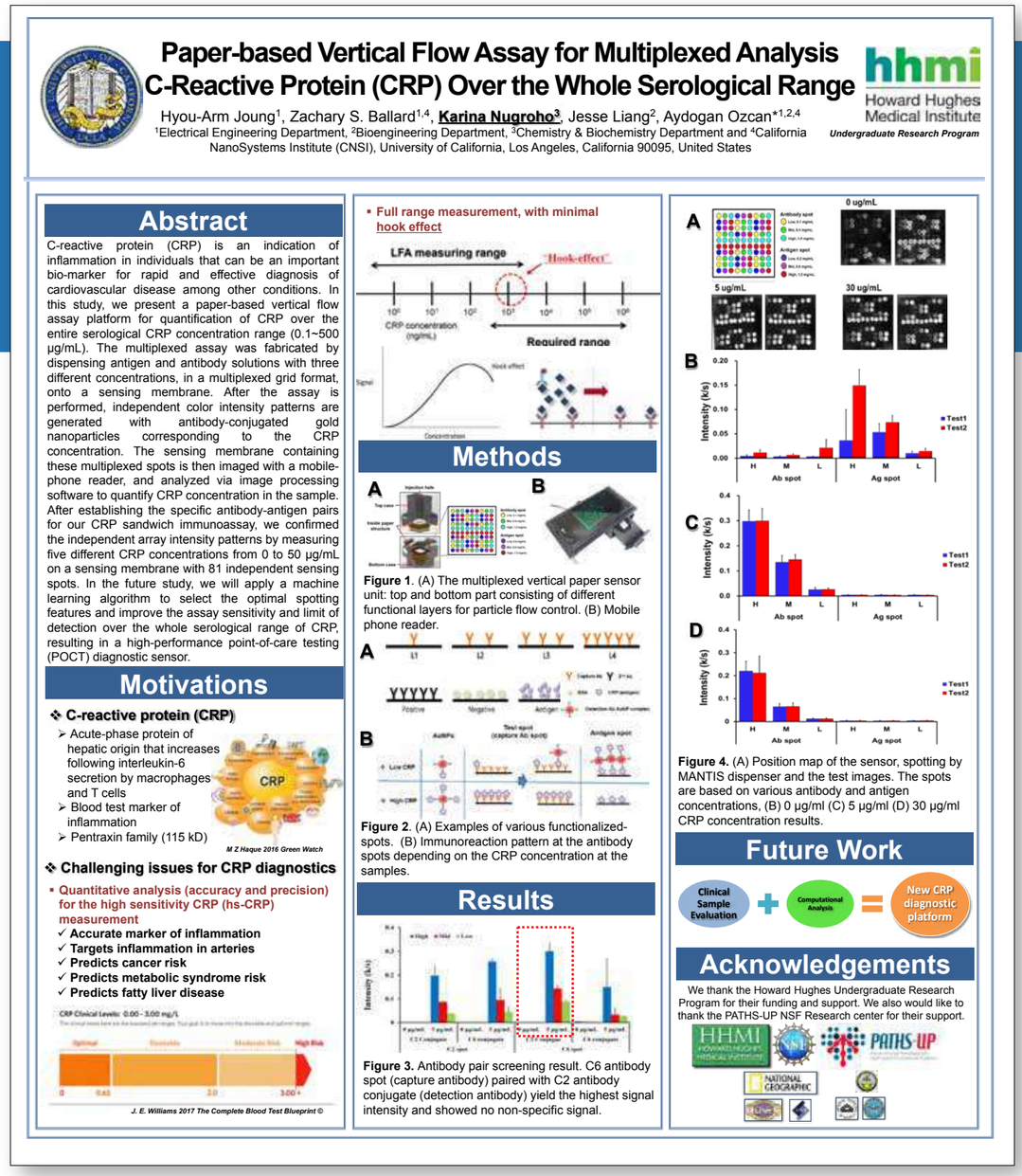

Paper-based Vertical Flow Assay for Multiplexed Analysis C-Reactive Protein (CRP) Over the Whole Serological Range

Hyou-Arm Joung[1], Zachary S. Ballard[1,4], **Karina Nugroho[3]**, Jesse Liang[2], Aydogan Ozcan*[1,2,4]

[1]Electrical Engineering Department, [2]Bioengineering Department, [3]Chemistry & Biochemistry Department and [4]California NanoSystems Institute (CNSI), University of California, Los Angeles, California 90095, United States

Howard Hughes Medical Institute — *Undergraduate Research Program*

Abstract

C-reactive protein (CRP) is an indication of inflammation in individuals that can be an important bio-marker for rapid and effective diagnosis of cardiovascular disease among other conditions. In this study, we present a paper-based vertical flow assay platform for quantification of CRP over the entire serological CRP concentration range (0.1~500 µg/mL). The multiplexed assay was fabricated by dispensing antigen and antibody solutions with three different concentrations, in a multiplexed grid format, onto a sensing membrane. After the assay is performed, independent color intensity patterns are generated with antibody-conjugated gold nanoparticles corresponding to the CRP concentration. The sensing membrane containing these multiplexed spots is then imaged with a mobile-phone reader, and analyzed via image processing software to quantify CRP concentration in the sample. After establishing the specific antibody-antigen pairs for our CRP sandwich immunoassay, we confirmed the independent array intensity patterns by measuring five different CRP concentrations from 0 to 50 µg/mL on a sensing membrane with 81 independent sensing spots. In the future study, we will apply a machine learning algorithm to select the optimal spotting features and improve the assay sensitivity and limit of detection over the whole serological range of CRP, resulting in a high-performance point-of-care testing (POCT) diagnostic sensor.

Motivations

❖ **C-reactive protein (CRP)**

- Acute-phase protein of hepatic origin that increases following interleukin-6 secretion by macrophages and T cells
- Blood test marker of inflammation
- Pentraxin family (115 kD)

M Z Haque 2016 Green Watch

❖ **Challenging issues for CRP diagnostics**

- **Quantitative analysis (accuracy and precision) for the high sensitivity CRP (hs-CRP) measurement**

✓ **Accurate marker of inflammation**
✓ **Targets inflammation in arteries**
✓ **Predicts cancer risk**
✓ **Predicts metabolic syndrome risk**
✓ **Predicts fatty liver disease**

J. E. Williams 2017 The Complete Blood Test Blueprint ©

- **Full range measurement, with minimal hook effect**

Methods

Figure 1. (A) The multiplexed vertical paper sensor unit: top and bottom part consisting of different functional layers for particle flow control. (B) Mobile phone reader.

Figure 2. (A) Examples of various functionalized-spots. (B) Immunoreaction pattern at the antibody spots depending on the CRP concentration at the samples.

Results

Figure 3. Antibody pair screening result. C6 antibody spot (capture antibody) paired with C2 antibody conjugate (detection antibody) yield the highest signal intensity and showed no non-specific signal.

Figure 4. (A) Position map of the sensor, spotting by MANTIS dispenser and the test images. The spots are based on various antibody and antigen concentrations, (B) 0 µg/ml (C) 5 µg/ml (D) 30 µg/ml CRP concentration results.

Future Work

Acknowledgements

We thank the Howard Hughes Undergraduate Research Program for their funding and support. We also would like to thank the PATHS-UP NSF Research center for their support.

Karunesh Sachanandani

Electrical Engineering

Freshman

LAB NAME

Structures-Computer Interaction Laboratory

FACULTY ADVISOR

Khalid Jawed

DAILY LAB SUPERVISOR

Weicheng Huang

DEPARTMENT

Mechanical and Aerospace Engineering

Directional Control of Flagellar Soft Robots through Buckling Instability

Rotation of a bacterium's flagella under high angular velocities results in a buckling effect. Our aim is to physically simulate the nature of this buckling effect. It is proposed that changes in the angular velocity of the flagella can affect the bacterium's trajectory. We attempt to model this motion on a larger scale by designing an autonomous soft robot. A microcontroller controlled via a Bluetooth module is used to drive a bipolar stepper motor and is placed in an ellipsoid shell. A flagella is manufactured using a polymer and is attached to the shell. The robot is then placed vertically in a tank filled with glycerin, the low Reynolds number fluid of choice for our large robot to mimic a bacterium in water. To verify the buckling effect, the flagella is made to rotate and its angular velocity is slowly increased. Initially, the robot should move predictably, with an upward force being generated. Above a critically angular velocity, a buckling effect is to be observed due to the instability through the fluid-structure interaction. As the angular velocity is then decreased to a constant value in the unbuckled domain, it is expected that the motion is stable once again and the robot continues to move in a straight line, albeit in a different direction. On a broader note, it is hypothesized that changes in the angular velocity alone can account for any trajectory. Such a model could account for the complex 3-dimensional motion of bacteria in viscous fluids.

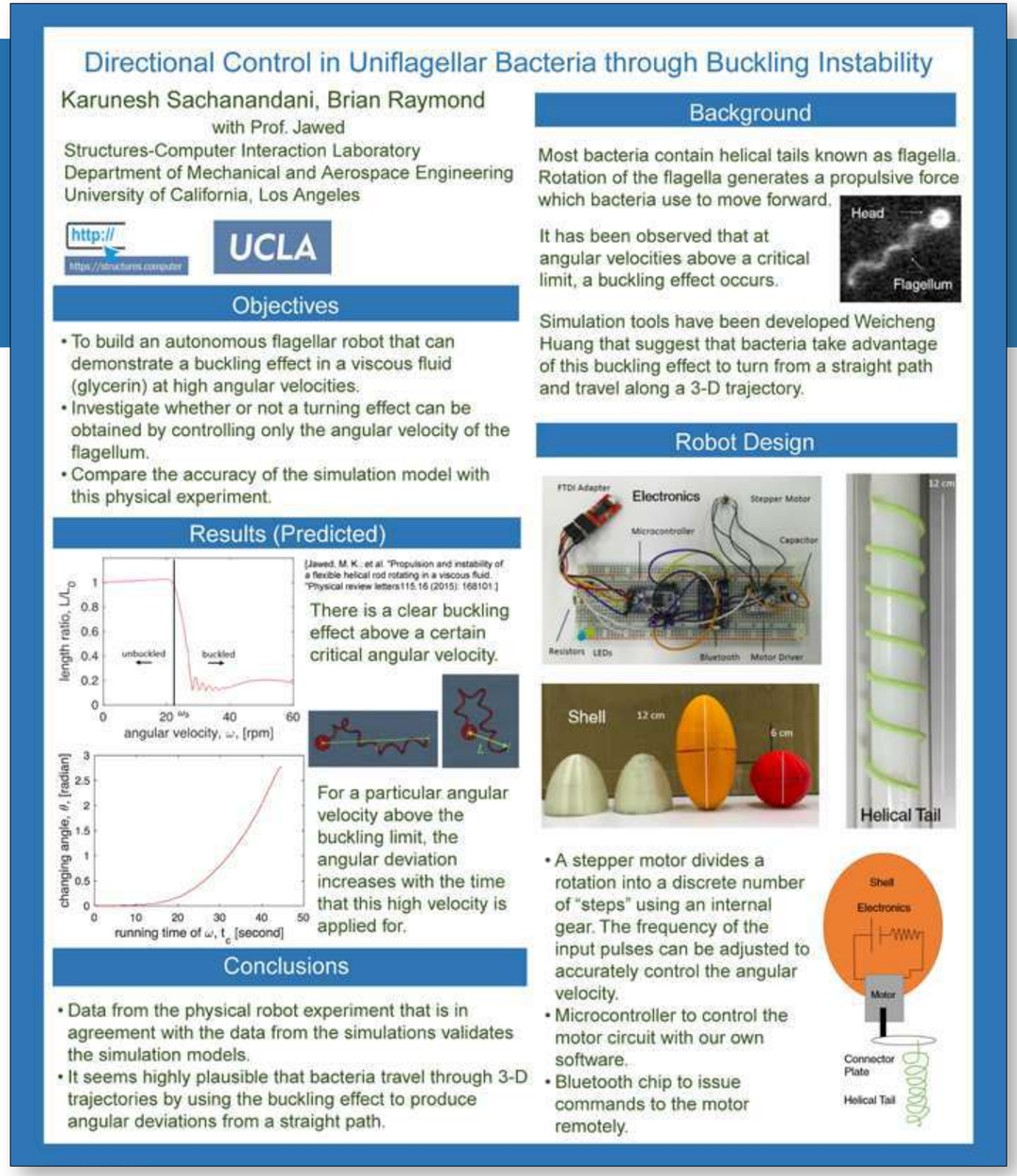

LAB NAME
Tang Lab

FACULTY ADVISOR
Yi Tang

DAILY LAB SUPERVISOR
Sunny Hung

DEPARTMENT
Chemical and Biomolecular Engineering

Alexander Soohoo

Chemical Engineering

Sophomore

Elucidation of the Biosynthesis of Brefeldin A with CRISPR/Cas9

Brefeldin A is a secondary metabolite first isolated from Penicillium brefeldianum in 1958. The compound is used in protein transport research and inhibits protein transport from the endoplasmic reticulum to the Golgi apparatus by targeting a guanine nucleotide exchange factor necessary for vesicle formation. This eventually leads to cell apoptosis, making it a compound of interest for cancer research. However, despite its importance, its biosynthesis is currently unknown and the gene cluster responsible for production is unconfirmed. This research hopes to solve the biosynthetic pathway of Brefeldin A through two complementary methods.

First, we will use heterologous expression using Penicillium expansum. Prior attempts at heterologous expression using Saccharomyces cerevisiae and Aspergillus nidulans were inconclusive. However, we believe use of a heterologous host of the same genus as the native organism will provide useful results. Additionally, we will attempt to solve the biosynthesis through genetic control of the original host. Although prior attempts to determine the gene cluster controlling Brefeldin A production were inconclusive, we have used CRISPR gene editing to positively identify Brefeldin A's gene cluster, and will use knockout strains to determine the biosynthetic pathway. Solving the biosynthesis of Brefeldin A will allow for development of more Brefeldin A derivatives, which have promising medicinal properties.

UCLA ENGINEERING
Henry Samueli School of Engineering and Applied Science

Elucidation of the Biosynthesis of Brefeldin A with CRISPR/Cas9

Alexander Soohoo, Yiu-Sun Hung, Yi Tang
Department of Chemical and Biomolecular Engineering. University of California, Los Angeles.
Los Angeles, CA 90095

Introduction

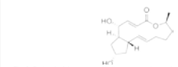

Fig. 1. Brefeldin A is a complex natural product used in protein transport research

What is Brefeldin A?

- Brefeldin A was isolated in 1958 from *P. brefeldianum,* and has many important chemical and medicinal properties, but has poor bio availability and is difficult to synthesize by organic chemists[1].
- Brefeldin A inhibits transport from the endoplasmic reticulum to the Golgi body by targeting the Guanine nucleotide exchange factor (GBF1), which is required for the formation of transport vesicles[2].
- The inhibition of the endomembrane system leads to apoptotic DNA fragmentation in the cell[1].
- The compound is very popular in protein transport, anti-cancer, and anti-mitotic research, and has great potential for new drugs.

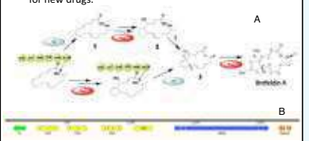

Fig. 2. This proposed biosynthetic pathway[3] is currently unconfirmed and still debated (A). This is the hypothesized and unconfirmed gene cluster responsible for Brefeldin A production (B).

What is the biosynthetic pathway of Brefeldin A?

- Although *P. brefeldianum* was discovered long ago and Brefeldin is an important chemical compound, its biosynthetic pathway is still unsolved.
- Fig 2. shows the current most-widely accepted biosynthetic pathway of Brefeldin A. Prior research using heterologous expression obtained Intermediate 1.[3]
- The proposed gene cluster is still unconfirmed.

Methods

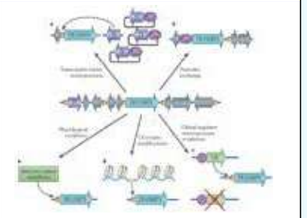

Fig. 3. There are two ways to solve the biosynthesis of fungal natural products: Genetic control in the original host[4] and heterologous expression

- *P. brefeldianum*, the native organism of Brefeldin A, was used to investigate the biosynthetic pathway.
- Epigenetic control of *P. brefeldianum* involved the insertion of a Zeocin antibiotic resistance marker through the use of CRISPR/Cas9.
- CRISPR/Cas9 cuts the genomic DNA and allows for insertion of the antibiotic resistance marker through homologous recombination.
- The *P. brefeldianum* strain with the Zeocin resistance was grown in media with Zeocin to identify which cells had the edited DNA.
- *P. expansum* was used through heterologous expression to investigate the biosynthetic pathway.
- Previous attempts at heterologous expression involved yeast[1], and *A. nidulans,* which led to no Brefeldin A production.
- It is hypothesized that a host of the same genus as the native organism will potentially lead to product of Brefeldin A or its intermediates.

Results

CRISPR/Cas9 Genomic Editing

Fig. 4. CRISPR/Cas9 was used to knockout the PKS gene and replace it with a genetic marker for antibiotic resistance.

- CRISPR/Cas9 was used to knockout the PKS gene in the gene cluster of interest, and replaced with a genetic marker for resistance to the antibiotic Zeocin.
- PCR was conducted to amplify the genetically modified DNA region.
- Gel electrophoresis analysis showed successful genetic manipulation of the DNA region.

LCMS Analysis of Compound Production

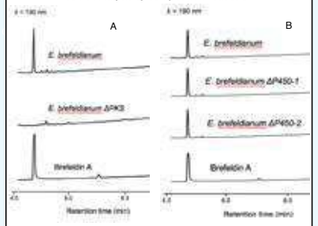

Fig. 5. LCMS analysis of compound production showed the lack of Brefeldin A production when the PKS gene was knocked out (A). Inconclusive results were obtained when two different P450 genes were knocked out (B).

- LCMS analysis confirms that the production of Brefeldin A by the native organism.
- LCMS analysis shows the lack of Brefeldin A production in *E. brefeldianum* that had the PKS in the specified gene cluster removed.
- Knockout of the individual P450-1 and P450-2 genes did not lead to abolishment of Brefeldin A production.
- However, hypothetically both P450-1 and P450-2 can have the same function and role in the biosynthetic pathway.

Heterologous Expression

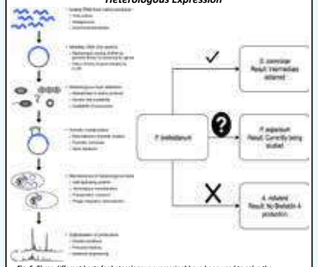

Fig. 6. Three different hosts for heterologous expression[5] have been used to solve the biosynthetic pathway of Brefeldin A.

- Heterologous expression in *A. nidulans* did not produce Brefeldin A.
- Heterologous expression in *S. cerevisiae* lead to production of Intemediate 1 of Brefeldin A.
- Heterologous expression in *P. expansum* is currently being investigated

Discussion

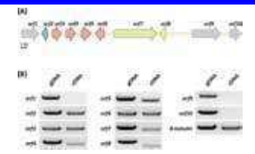

Fig. 7. RT-PCR suggested the boundary of the gene cluster for Brefeldin A[3].

- RT-PCR uses cDNA as an identifier for which genes are involved in the production of Brefeldin A.
- From the previously hypothesized gene cluster, seven genes were identified as genes of interest.
- The PKS gene is responsible for creating the scaffold backbone of Brefeldin A, and the compound cannot be synthesized when the PKS enzyme is absent.
- The absence of Brefeldin A provides the strongest evidence yet to confirm the hypothesized gene cluster[3] responsible for compound production.
- Past research using *A. nidulans* did not produce Brefeldin A. Although there are typically gene clusters responsible for compound production, there are other proteins in the cell that can aid compound production.
- It is hypothesized that use of a host of the same genus as the native organism in heterologous expression will lead to helpful results.
- Three of the seven genes of interest have investigated, and the remaining four genes are currently being researched.

ORF	Predicted function
1	Thiohydrolase
2	P450
3	P450
4	P450
5	P450
6	HRPKS
7	Unknown

Fig. 8. Three genes have been investigated using knockout strain of the native host (orange). Four genes are currently being researched (blue).

Conclusions

- The use of CRISPR/Cas9 provides the strongest evidence yet of the gene cluster of interest's role in the production of Brefeldin A.
- Genetic control of the individual host indicate two genes' lack of participation in the biosynthetic pathway.
- Future research will knockout the remaining genes in the studied gene cluster.
- Heterologous expression in *P. expansum* will provide complementary analysis of the biosynthetic pathway.
- It is anticipated that subsequent research will elucidate the biosynthetic pathway of Brefeldin A or lead to discovery of more derivatives or intermediates.

Acknowledgements and References

- Thank you to Professor Yi Tang and Yiu-Sun Hung for providing guidance and mentorship on this project.
- Thank you to the UCLA HSSEAS Undergraduate Research Program for providing support and guidance in presentation of undergraduate research.

[1] He, B., Wang, Y., Zheng, Y., et. al. (2013). Synthesis and cytotoxic evaluation of acylated brefeldin a derivatives as potential anticancer agents. *Chem Biol Drug Des*, *82*, 207-216. doi: 10.1111/cbdd.12154.

[2] Seehafer, K., Rominger, F., Helmchen, G., Langhans, M. et. al. (2013). Synthethis and Biological Properties of Novel Brefeldin A Analogues. *J. Med. Chem., 56* (14), 5872-5884. doi: 10.1021/jm400615g

[3] Zabala, A., Chooi, Y, Choi, M., et. al. (2014). Fungal Polyketide Synthase Product Chain-Length Control by Partnering Thiohydrolase. *ACS Chemical Biology, 9* (7), 1576-1586. doi: 10.1021/cb5002841

[4] Brakhage, A. Regulation of Fungal Secondary Metabolism. *Nature Reviews Microbiology, 11*, 21-32. doi: 10.1038/nrmicro2916

[5] Ongley, S., Bian, X., Neilan, B., et. al (2013). Recent advances in the heterologous expression of microbial natural product. *Nat. Prod. Rep.* 30, 1121–1138. doi: 10.1039/c3np70034h

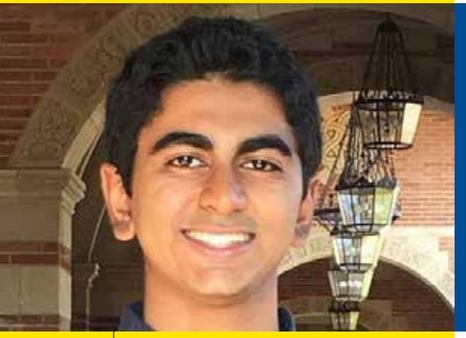

Yashes Srinivasan

Bioengineering

Junior

LAB NAME

Wong Research Lab

FACULTY ADVISOR

Gerard Wong

DAILY LAB SUPERVISOR

Ernest Lee

DEPARTMENT

Bioengineering

Mechanism of Amyloid-Mediated Cellular Toxicity via Mitochondria Disruption Corresponds to Mitochondrial Membrane Curvature Generation

Amyloid peptides and fibrils are implicated in the pathogenesis of neurodegenerative diseases such as Alzheimer's disease. Recent work has proposed that amyloids induce neurotoxicity by permeating neuronal plasma membranes1,2. However, biochemical studies have shown that amyloids are also associated with mitochondrial dysfunction and disruption of cellular metabolism in neurons3. In this study, we hypothesize that amyloid peptides and fibrils induce mitochondrial dysfunction by directly permeabilizing mitochondrial membranes. Interestingly, unrelated proteins such as the molecular motor Dnm14 and Bcl-2-associated X protein (BAX) have previously been shown to be capable of deforming mitochondrial cell membranes for processes such as fission and induction of apoptosis5. Using small angle X-ray scattering (SAXS), we demonstrate that the peptide and fibril forms of amyloids Aβ, Aβ Arctic and R3 Tau induce negative Gaussian curvature (NGC) in mitochondrial membranes under physiological conditions, both in the presence and absence of calcium. NGC is a topological criterion for membrane permeation events in both bacterial6 and mitochondrial4 cell membranes. These, results suggest that amyloid fibrils formed during the disease state can directly penetrate mitochondrial membranes, resulting in mitochondrial dysfunction and neurotoxicity. Antagonizing amyloid-mediated disruption of mitochondrial membranes may offer a therapeutic strategy for the treatment of neurodegenerative diseases.

Mechanism of amyloid-mediated cellular toxicity via mitochondrial disruption corresponds to membrane curvature generation

Yashes Srinivasan[1], Ernest Y. Lee[1], Ghee Hwee Lai[1], Gerard C.L. Wong[1*]

[1]Department of Bioengineering, UCLA, Los Angeles, CA

*gclwong@seas.ucla.edu

UCLA | Samueli School of Engineering

HSSEAS Undergraduate Research Program

Introduction

Background

- Amyloids are insoluble fibrous protein strands particularly associated with neurodegenerative diseases such as Alzheimer's disease, although the precise mechanism of pathogenesis is still unclear
- Biochemical studies have shown that amyloids are imported into the mitochondria and associated with mitochondrial dysfunction and disruption of cellular metabolism in neurons

Hypothesis

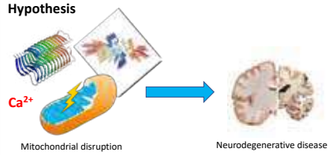

- In this study, we hypothesize that peptide and fibril forms of amyloids Aβ, APP Arctic, and R3 Tau induce mitochondrial dysfunction and cell degeneration by generating negative Gaussian curvature in order to directly permeabilize mitochondrial membranes
- In addition, calcium may play a role in this process

Negative Gaussian Curvature (NGC)

- NGC, or "saddle-splay" curvature, is a topological criterion for membrane permeation and deformation events in both bacterial and mitochondrial cell membranes

Importance of Calcium (Ca^{2+})

- Ca^{2+} is a physiologically relevant divalent cation
- Amyloids been shown to interact with divalent cations, modulating their structure and function

References

Mattson, M. P., Tomaselli, K. J. & Rydel, R. E. Calcium-destabilizing and neurodegenerative effects of aggregated β-amyloid peptide are attenuated by basic FGF. *Brain Res.* **621**, 35–49 (1993).
Rambaran, R. N. & Serpell, L. C. Amyloid fibrils: abnormal protein assembly. *Prion* **2**, 112–7 (2008).
Reddy, P. H. Abnormal tau, mitochondrial dysfunction, impaired axonal transport of mitochondria, and synaptic deprivation in Alzheimer's disease. *Brain Res.* **1415**, 136–48 (2011).
Schmidt, N. W. *et.al.* Influenza Virus A M2 Protein Generates Negative Gaussian Membrane Curvature Necessary for Budding and Scission. *J. Am. Chem. Soc.* **135**, 13710–13719 (2013)
Chen, J. X. *et.al.* Amyloid-β-Induced Mitochondrial Dysfunction. *J. Alzheimer's Dis.* **12**, 177–184 (2007).
Williams, T. L. & Serpell, L. C. Membrane and surface interactions of Alzheimer's Aβ peptide - insights into the mechanism of cytotoxicity. *FEBS J.* **278**, 3905–3917 (2011).

Y.S. thanks HSSEAS URP, E.Y.L and G.C.L.W. for mentorship and support. Synchrotron experiments were conducted by E.Y.L and G.H.L. Amyloid peptides were provided by N.W. Schmidt and W.F. Degrado. X-ray research was conducted at Stanford Synchrotron Radiation Light Source, SLAC National Laboratory, supported by the US DOE Office of Basic Energy Sciences under Contract No. DE-AC02-76SF00515

Materials and Methods

Experimental Details

- We solved structures of amyloid peptides in complex with liposomes mimicking mitochondrial membranes using small-angle-X-ray-scattering (SAXS) at physiologically relevant stoichiometries
- We prepared samples containing Ca^{2+} and samples lacking Ca^{2+}

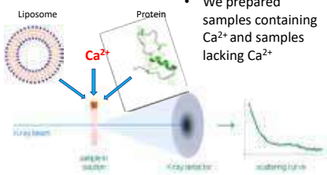

X-Ray Diffraction Pattern Analysis

- We analyzed diffraction peaks in the scattering curves to determine if NGC was present
- The presence of NGC can be determined by recognizing cubic phases in solution. Cubic phases are indicated by characteristic ratios between diffraction peaks of √2 : √3 : √4 : √6 : √8 : √9 : √10 : √12. The cubic phase lattice parameter is calculated as $a = 2\pi\sqrt{2}/q_{110}$

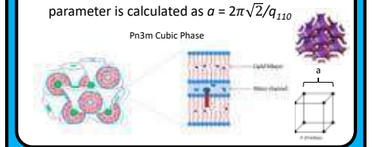

Result 1: Aβ peptide and fibril generate NGC in mitochondrial membranes

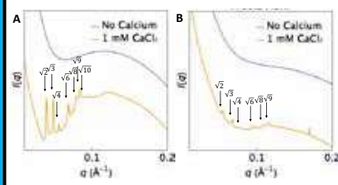

(A) SAXS data for Aβ peptide complexed with liposomal mitochondrial membrane indicates that Aβ peptide induces Pn3m cubic phase in the presence of calcium due to presence of the characteristic ratios. The lattice parameter is a = 22.4 nm in the presence of Ca^{2+}. **(B)** SAXS data for Aβ fibril complexed with liposomal mitochondrial membranes indicates that Aβ fibril induces Pn3m cubic phase in the presence of calcium due to the presence of the characteristic ratios. The lattice parameter is a = 16.0 nm in the presence of Ca^{2+}.

Result 2: APP Arctic peptide and fibril generate NGC in mitochondrial membranes

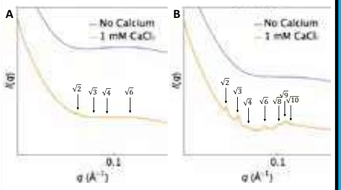

(A) SAXS data for APP Arctic peptide complexed with liposomal mitochondrial membrane indicates that APP Arctic peptide induces Pn3m cubic phase in the presence of calcium due to presence of the characteristic ratios. The lattice parameter is a = 17.6 nm in the presence of Ca^{2+}. **(B)** SAXS data for APP Arctic fibril complexed with liposomal mitochondrial membranes indicates that APP Arctic fibril induces Pn3m cubic phase in the presence of calcium due to the presence of the characteristic ratios. The lattice parameter is a = 17.4 nm in the presence of Ca^{2+}.

Result 3: R3 tau peptide and fibril generate NGC in mitochondrial membranes

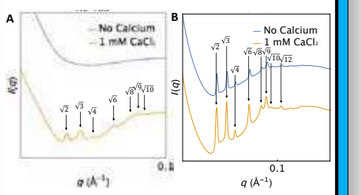

(A) SAXS data for R3 Tau peptide complexed with liposomal mitochondrial membrane indicates that R3 Tau peptide induces Pn3m cubic phase in the presence of calcium due to presence of the characteristic ratios. The lattice parameter is a = 21.7 nm for the in the presence of Ca^{2+}. **(B)** SAXS data for R3 Tau fibril complexed liposomal mitochondrial membranes indicates that R3 Tau fibril induces Pn3m cubic phase due to the presence of the characteristic ratios. The lattice parameter is a = 20.9 nm in the presence and absence of Ca^{2+}.

Conclusions and Future Directions

- The pathophysiological mechanism of amyloids in cell degeneration is partly associated with mitochondrial membrane destabilizing and permeabilizing activity
- Future experiments include antagonizing NGC formation to test for reduced cellular toxicity and determining if other amyloid peptides also deform mitochondrial membranes

Katherine Tsai

Biochemistry

Junior

LAB NAME

The Ozcan Research Group

FACULTY ADVISOR

Aydogan Ozcan

DAILY LAB SUPERVISOR

Yibo Zhang

DEPARTMENT

Electrical Engineering

Circulating Tumor Cell Detection in Blood Using Magnetically Enhanced Lens-Free Imaging

Approximately 90% of cancer-related deaths are due to metastasis, the development of secondary malignant growths at a distance from a primary site of cancer. Therefore, early diagnosis and treatment is the key to reducing cancer deaths. Before a tumor metastasizes, it releases circulating tumor cells (CTCs) into the blood which can be detected by liquid biopsy. Here, a novel imaging technique was developed to detect individual CTCs from whole blood with a low limit of detection using magnetically enhanced lens-free imaging. Antibody-coated superparamagnetic beads were used to specifically label the cancer cells in blood, and an alternating magnetic field was used to induce oscillatory motion to the labeled cells. Lens-free microscopes were used to record the time-varying diffraction patterns, and a computational algorithm created contrast from the oscillatory motion through differential image analysis. Blood samples with MCF7 cells harvested from a human breast cancer patient were used to optimize the magnetic labeling protocol of the cancer cells. Proof of concept has been established for the detection of magnetically labeled cancer cells in phosphate buffer solution. Oscillatory motion has been observed using a benchtop bright-field microscope and a lens-free microscope with a computational motion analysis algorithm. Future optimization needs to be performed to label cancer cells in whole blood.

Rare Cell Detection in Bodily Fluids Using Magnetically Enhanced Lens-Free On-Chip Imaging

Yibo Zhang[1,2,3], Aniruddha Ray[1,2,3], Janay Kong[2], Donghyuk Kim[2], Kahlen Ouyang[2], Katherine Tsai[4], Xuewei Liu[1], Danny Kim[2], Alex Guziak[5], Hatice Ceylan Koydemir[1,2,3], Omai Garner[6], Dino Di Carlo[2], and Aydogan Ozcan[1,2,3,7]

[1]Electrical and Computer Engineering Department, UCLA; [2]Bioengineering Department, UCLA; [3]California NanoSystems Institute (CNSI), UCLA; [4]Biochemistry Department, UCLA; [5]Physics Department, UCLA; [6]Department of Pathology & Laboratory Medicine, UCLA; [7]Department of Surgery, David Geffen School of Medicine, UCLA

Introduction

Approximately 90% of cancer-related deaths are due to metastasis, the development of secondary malignant growths at a distance from a primary site of cancer[1]. Therefore, early diagnosis and treatment is the key to reducing cancer deaths. Before a tumor metastasizes, it will release circulating tumor cells (CTCs) into the blood which can be detected by liquid biopsy. Many CTCs express cell surface markers called epithelial cell adhesion molecules (EpCAMs)[2]. Some research has already been done using small magnetic beads conjugated to anti-EpCAM antibodies in order to identify and separate CTCs from blood samples. However, CTCs are extremely rare: the presence of one or more CTCs in 7.5 mL of blood in a breast cancer patient is a predictor of decreased progression-free and overall survival[3]. Existing techniques use magnetic beads to label and enrich CTCs for their detection, but are limited by failure to detect these low levels of CTCs.

Here, we try to develop a novel imaging technique to detect individual CTCs from whole blood with a low limit of detection using magnetically enhanced lens-free imaging. We use antibody-coated superparamagnetic beads to specifically label the cancer cells in blood, and use an alternating magnetic field to induce oscillatory motion to the labeled cells. Lens-free microscopes will be used to record the time-varying diffraction patterns, and a computational algorithm will create contrast from the oscillatory motion through differential image analysis.

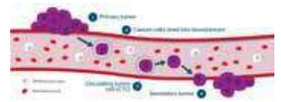

Fig. 1. Tumor metastasis.[4]

Materials and Methods

Optimization of protocol of the labeling of MCF7 cells
Whole blood samples with cultured MCF7 cells were used. The cancer cells were tagged with anti-EpCAM magnetic beads. Tests were performed in PBS to optimize the labeling of CTCs with magnetic beads. In order to determine the optimal cancer cell to magnetic bead ratio, various ratios were tried, including 50:1, 100:1, 200:1, and 400:1.

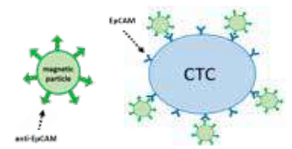

Fig. 2. Anti-EpCAM magnetic labeling of CTC.

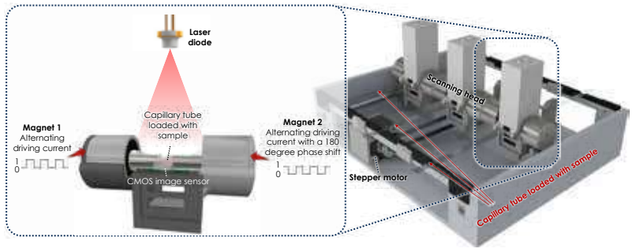

Fig. 3. Device schematic with three lens-free microscopes scanning three capillary tubes in parallel.

Digital acquisition of images/videos
A Windows-based application graphical user interface (GUI) was programmed to provide a user-friendly interface which allows the user to initiate the test on the device and then allow the data to be analyzed. The final program incorporated digital back-propagation of the captured image sequence, differential analysis at different time intervals, image segmentation to detect the signals of interest, and a machine learning algorithm that rejects potential false positive detections.

Results and Discussion

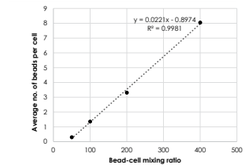

Fig. 4. The number of magnetic beads labeling the tumor cells using different bead-cell mixing ratios.

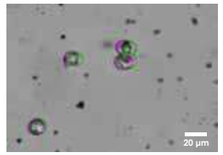

Fig. 5. Oscillation of magnetically labeled cancer cells under an alternating magnetic field, captured by a benchtop 20x bright-field microscope. This is a composite image of two images taken at the extreme positions of one oscillation period. The two extremes overlay in green and magenta.

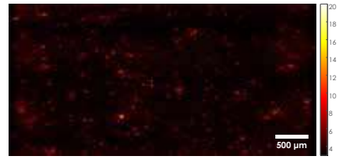

Fig. 6. Image acquired by the lens-free on-chip microscope, after applying a computational motion analysis algorithm. Hotspots correspond to particles with oscillatory motion.

Conclusion

- We propose a technique of using magnetically induced oscillatory motion as a novel biomarker to detect rare cells in bodily fluids such as the blood.
- Optimization of magnetic labeling of MCF7 cancer cells has been conducted in PBS. Future optimization needs to be performed to label cancer cells in whole blood.
- Oscillatory motion has been observed using a benchtop bright-field microscope. It is also observed using a lens-free microscope with a computational motion analysis algorithm.

Reference

[1]Seyfried, T. N., & Huysentruyt, L. C. (2013). On the Origin of Cancer Metastasis. *Critical Reviews in Oncogenesis*, *18*(1-2), 43–73.
[2]deWit, S., van Dalum, G., Lenferink, A.T.M., et al. (2015). The detection of EpCAM+ and EpCAM- circulating tumor cells. *Scientific Reports*, *5*, 12270. doi:10.1038/srep12270
[3]Xenidis, N., et al. (2013). Differential effect of adjuvant taxane-based and taxane-free chemotherapy regimens on the CK-19 mRNA-positive circulating tumour cells in patients with early breast cancer. *British Journal of Cancer*, *108*(3), 549–556. http://doi.org/10.1038/bjc.2012.597
[4]Liquid Biopsies: New Technology Uses a Microfluidic Vortex to Isolate Circulating Tumor Cells (CTCs) from Blood Samples. *Society for Laboratory Automation and Screening*. 10 April 2017.

Acknowledgement

Peter Wang

Chemical Engineering

Sophomore

LAB NAME

Nanoscale Biotic-Abiotic Systems Engineering Laboratory

FACULTY ADVISOR

Dean Ho

DAILY LAB SUPERVISOR

Theodore Kee

DEPARTMENT

Bioengineering

Comprehensive Analysis of Nanodiamond-Antibiotic/Doxorubicin Multi-Drug Loading and Elution

Nanodiamonds (NDs) have been extensively explored in biomedical applications due to their favorable properties, such as biocompatibilities and diverse surface electrostatics that allow rapid conjugations with drugs. Enhancing chemotherapeutic efficacy through optimized nanodiamond drug delivery system would further improve the treatment of cancers. In this study, carboxylated nanodiamonds and original nanodiamonds were involved to explore the maximum efficiency in binding and release capability of doxorubicin (DOX). The binding ratio of NDs and DOX, pH values, and release time were optimized. Notably, an NDX synthesized in 2 mL ND, 5 mL DOX, and 0.061 mL NaOH exhibits a ~63.4% (31.7 wt%) binding efficiency, and NDX release profile quantified in acidic environment exhibits ~99.9% release efficiency of DOX. The present work establishes a foundation for future applications in drug delivery system for enhancing chemotherapy efficacy.

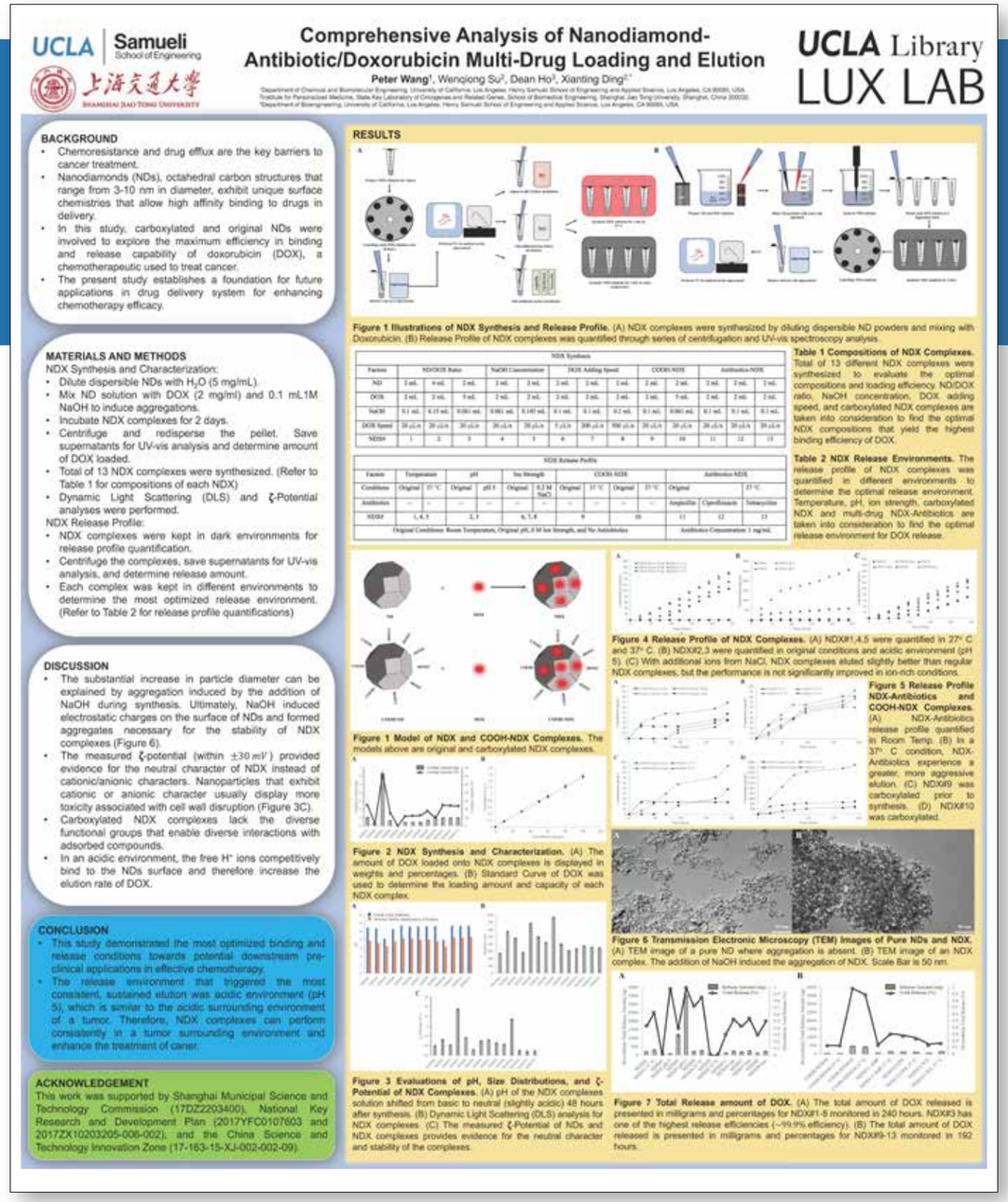

UCLA Samueli School of Engineering | 上海交通大学 SHANGHAI JIAO TONG UNIVERSITY

Comprehensive Analysis of Nanodiamond-Antibiotic/Doxorubicin Multi-Drug Loading and Elution

Peter Wang[1], Wenqiong Su[2], Dean Ho[3], Xianting Ding[2,*]

[1]Department of Chemical and Biomolecular Engineering, University of California, Los Angeles, Henry Samueli School of Engineering and Applied Science, Los Angeles, CA 90095, USA
[2]Institute for Personalized Medicine, State Key Laboratory of Oncogenes and Related Genes, School of Biomedical Engineering, Shanghai Jiao Tong University, Shanghai, China 200030
[3]Department of Bioengineering, University of California, Los Angeles, Henry Samueli School of Engineering and Applied Science, Los Angeles, CA 90095, USA

UCLA Library LUX LAB

BACKGROUND

- Chemoresistance and drug efflux are the key barriers to cancer treatment.
- Nanodiamonds (NDs), octahedral carbon structures that range from 3-10 nm in diameter, exhibit unique surface chemistries that allow high affinity binding to drugs in delivery.
- In this study, carboxylated and original NDs were involved to explore the maximum efficiency in binding and release capability of doxorubicin (DOX), a chemotherapeutic used to treat cancer.
- The present study establishes a foundation for future applications in drug delivery system for enhancing chemotherapy efficacy.

MATERIALS AND METHODS

NDX Synthesis and Characterization:

- Dilute dispersible NDs with H_2O (5 mg/mL).
- Mix ND solution with DOX (2 mg/ml) and 0.1 mL1M NaOH to induce aggregations.
- Incubate NDX complexes for 2 days.
- Centrifuge and redisperse the pellet. Save supernatants for UV-vis analysis and determine amount of DOX loaded.
- Total of 13 NDX complexes were synthesized. (Refer to Table 1 for compositions of each NDX)
- Dynamic Light Scattering (DLS) and ζ-Potential analyses were performed.

NDX Release Profile:

- NDX complexes were kept in dark environments for release profile quantification.
- Centrifuge the complexes, save supernatants for UV-vis analysis, and determine release amount.
- Each complex was kept in different environments to determine the most optimized release environment. (Refer to Table 2 for release profile quantifications)

DISCUSSION

- The substantial increase in particle diameter can be explained by aggregation induced by the addition of NaOH during synthesis. Ultimately, NaOH induced electrostatic charges on the surface of NDs and formed aggregates necessary for the stability of NDX complexes (Figure 6).
- The measured ζ-potential (within $\pm 30\ mV$) provided evidence for the neutral character of NDX instead of cationic/anionic characters. Nanoparticles that exhibit cationic or anionic character usually display more toxicity associated with cell wall disruption (Figure 3C).
- Carboxylated NDX complexes lack the diverse functional groups that enable diverse interactions with adsorbed compounds.
- In an acidic environment, the free H^+ ions competitively bind to the NDs surface and therefore increase the elution rate of DOX.

CONCLUSION

- This study demonstrated the most optimized binding and release conditions towards potential downstream preclinical applications in effective chemotherapy.
- The release environment that triggered the most consistent, sustained elution was acidic environment (pH 5), which is similar to the acidic surrounding environment of a tumor. Therefore, NDX complexes can perform consistently in a tumor surrounding environment and enhance the treatment of caner.

ACKNOWLEDGEMENT

This work was supported by Shanghai Municipal Science and Technology Commission (17DZZ2203400), National Key Research and Development Plan (2017YFC0107603 and 2017ZX10203205-006-002), and the China Science and Technology Innovation Zone (17-163-15-XJ-002-002-09).

RESULTS

Figure 1 Illustrations of NDX Synthesis and Release Profile. (A) NDX complexes were synthesized by diluting dispersible ND powders and mixing with Doxorubicin. (B) Release Profile of NDX complexes was quantified through series of centrifugation and UV-vis spectroscopy analysis.

Table 1 Compositions of NDX Complexes. Total of 13 different NDX complexes were synthesized to evaluate the optimal compositions and loading efficiency. ND/DOX ratio, NaOH concentration, DOX adding speed, and carboxylated NDX complexes are taken into consideration to find the optimal NDX compositions that yield the highest binding efficiency of DOX.

Table 2 NDX Release Environments. The release profile of NDX complexes was quantified in different environments to determine the optimal release environment. Temperature, pH, ion strength, carboxylated NDX and multi-drug NDX-Antibiotics are taken into consideration to find the optimal release environment for DOX release.

Figure 1 Model of NDX and COOH-NDX Complexes. The models above are original and carboxylated NDX complexes.

Figure 4 Release Profile of NDX Complexes. (A) NDX#1,4,5 were quantified in 27° C and 37° C. (B) NDX#2,3 were quantified in original conditions and acidic environment (pH 5). (C) With additional ions from NaCl, NDX complexes eluted slightly better than regular NDX complexes, but the performance is not significantly improved in ion-rich conditions.

Figure 5 Release Profile NDX-Antibiotics and COOH-NDX Complexes. (A) NDX-Antibiotics release profile quantified in Room Temp. (B) In a 37° C condition, NDX-Antibiotics experience a greater, more aggressive elution. (C) NDX#9 was carboxylated prior to synthesis. (D) NDX#10 was carboxylated.

Figure 2 NDX Synthesis and Characterization. (A) The amount of DOX loaded onto NDX complexes is displayed in weights and percentages. (B) Standard Curve of DOX was used to determine the loading amount and capacity of each NDX complex.

Figure 6 Transmission Electronic Microscopy (TEM) Images of Pure NDs and NDX. (A) TEM image of a pure ND where aggregation is absent. (B) TEM image of an NDX complex. The addition of NaOH induced the aggregation of NDX. Scale Bar is 50 nm.

Figure 3 Evaluations of pH, Size Distributions, and ζ-Potential of NDX Complexes. (A) pH of the NDX complexes solution shifted from basic to neutral (slightly acidic) 48 hours after synthesis. (B) Dynamic Light Scattering (DLS) analysis for NDX complexes. (C) The measured ζ-Potential of NDs and NDX complexes provides evidence for the neutral character and stability of the complexes.

Figure 7 Total Release amount of DOX. (A) The total amount of DOX released is presented in milligrams and percentages for NDX#1-8 monitored in 240 hours. NDX#3 has one of the highest release efficiencies (~99.9% efficiency). (B) The total amount of DOX released is presented in milligrams and percentages for NDX#9-13 monitored in 192 hours.

LAB NAME
Wu Lab

FACULTY ADVISOR
Benjamin Wu

DAILY LAB SUPERVISOR
Chase Linsley

DEPARTMENT
Bioengineering

Max Zhu

Bioengineering

Junior

Preparation of Photothermal Palmitic Acid/ Cholesterol Liposomes

Indocyanine green (ICG) is the only FDA approved near-infrared dye and it is currently used clinically for diagnostic applications. However, there is significant interest in using ICG for triggered drug delivery applications and heat ablation therapy. Unfortunately, free ICG has a short half-life in vivo and is rapidly cleared from circulation. Liposomes have been frequently used to improve ICG's stability and overall time of effectiveness in vivo, but they have limited stability due to the susceptibility of phospholipids to hydrolysis and oxidation. In this study, non-phospholipid liposomes were used to encapsulate ICG, and the resulting liposomes were characterized for size, encapsulation efficiency, stability, and photothermal response. Using the thin-film hydration method, an ICG encapsulation efficiency of 54% was achieved, and the liposomes were stable for up to 12 weeks, with detectable levels of encapsulated ICG up to week 4. Additionally, ICG-loaded liposomes were capable of rapidly producing a significant photothermal response upon exposure to near infrared light, and this photothermal response was able to induce changes in the mechanical properties of thermally-responsive hydrogels. These chromophore-loaded liposomes have the potential to be tailored for a variety of applications, including triggered drug delivery, in vivo imaging and thermal ablation therapy.

Preparation of Photothermal Palmitic Acid/Cholesterol Liposomes

Max J. Zhu[1], Chase S. Linsley[1], Viola Y. Quach[1], and Benjamin M. Wu[1,2]

1. Department of Bioengineering, University of California, Los Angeles, Los Angeles, CA 90095, USA
2. Division of Advanced Prosthodontics and the Weintraub Center for Reconstructive Biotechnology, University of California, Los Angeles, Los Angeles, CA 90095, USA

INTRODUCTION

- Fluorescent molecules can be used to trigger drug release or ablate tissue to targeted areas in the body
- Indocyanine Green (ICG) is a chromophore that absorbs in the near infrared (NIR) region of light, which is permeable through the body
- Nonphospholipid liposomes can stabilize ICG from high clearance and hydrolysis rates

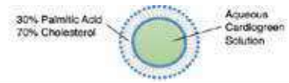

MATERIALS AND METHODS

- Liposomes were prepared using a **3:7 molar ratio** of palmitic acid:chlesterol subjected to the **thin-film hydration method** and hydrated with 0.2 mg/mL ICG solution
- **Absorption spectra** was measured via spectrophotometer
- Stability over time was recorded using **dynamic light scattering**
- **Encapsulation efficiency** was obtained by lysing liposomes and measuring absorbance of encapsulated ICG
- **Photothermal response** was measured by irradiating liposomes with NIR light (780 nm) and measuring temperature change after 2 minutes
- Proof of **mechanical changes in drug delivery vehicles** was modeled by loading gelatin with liposomes and inducing melting, tracked via **rheology**

HEAT GENERATION AND ENCAPSULATION

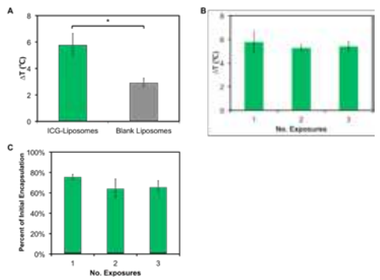

- ICG Liposomes are able to generate 5°C increase in temperature, which can trigger tissue ablation (A)
- Temperature change is consistent with multiple exposures, meaning liposomes are reusable (B)
- About 20% loss of encapsulated ICG after initial light exposure, but then insignificant loss after subsequent exposures (C)
- Further experimentation needed to prove that temperature change still occurs when encapsulated by a polymer

LIPOSOME PROPERTIES

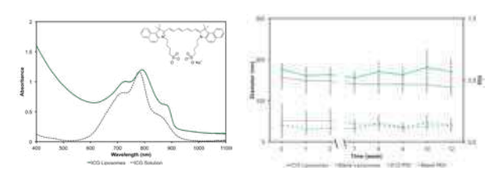

- ICG absorbance spectra experiences slight red shift upon encapsulation, moving peak absorbance deeper into the NIR light region (left)
- Liposome diameter and polydispersity index (PdI) does notsignificantly change over 12 weeks, suggesting stability of liposomes (right)

MECHANICAL CHANGE IN DRUG DELIVERY VEHICLES

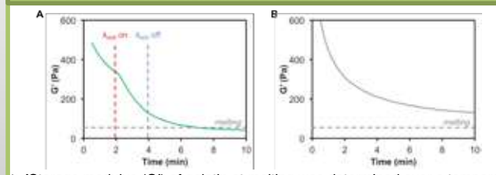

- Storage modulus (G') of gelatin at melting was determined over a temperature ramp from 25°C to 35°C
- Gelatin loaded with liposomes were able to reach melting G' (A), but blank gelatin exposed to NIR light did not (B)

CONCLUSION

- Palmitic acid/cholesterol liposomes are effective in stabilizing ICG *in vivo* with minimal changes in optical properties
- Liposomes can generate a reproducible temperature increase
- Liposomes can successfully induce temperature-dependent mechanical changes in model drug delivery vehicles

ACKNOWLEDGMENTS

Thank you to Wu Lab for supporting the project and to the Undergraduate Research Program for offering guidance in making this poster

If you would like to find out more about the Undergraduate Research Program,
please contact Director William Herrera:

William Herrera
Director
Undergraduate Research Program
310.825.9478
williamh@seas.ucla.edu
6288 Boelter Hall

Or visit our website at https://tinyurl.com/uclaurp.

UCLA Samueli School of Engineering

UCLA Samueli
School of Engineering

Office of Academic and Student Affairs
UCLA Samueli School of Engineering
420 Westwood Plaza, 6288 Boelter Hall, Los Angeles, CA, 90095-1600
310.825.9478 | www.samueli.ucla.edu